Int. J. of Precis. Eng. and Manuf.-Green Tech.
https://doi.org/10.1007/s40684-025-00837-7

Online ISSN 2198-0810
Print ISSN 2288-6206

REGULAR PAPER

Gold nanoparticles synthesized by laser ablation in saline medium: an assessment of colloidal stability

Philipi Cavalcante Ricardo[1] · Caio Raphael Vanoni[2] · Maurício Jeomar Piotrowski[3] · Daniel Coutinho Costa[4] · Jorge Padrão[5] · Andrea Zille[5] · Veronica Satulu[6] · Gheorghe Dinescu[6] · Óscar Carvalho[4] · Cristiane Luisa Jost[2] · Filipe Samuel Silva[4] · Marcio Celso Fredel[1]

Received: 1 September 2025 / Revised: 12 November 2025 / Accepted: 19 December 2025
© The Author(s), under exclusive licence to Korean Society for Precision Engineering 2026

Abstract

Gold nanoparticles (AuNPs) produced via pulsed laser ablation in liquids (PLAL) offer significant advantages due to their high purity and absence of ligands. However, their long-term stability is often compromised by aggregation and colloidal destabilization, which are not yet fully understood. This study investigates the influence of different saline agents (NaCl, $NaNO_3$, Na_2SO_3) and storage conditions on the stabilization of PLAL-produced AuNPs over three months. The nanoparticles were characterized using UV-Vis spectroscopy, XRD, ZP, DLS, XPS, and HRTEM, while computational studies based on density functional theory (DFT) explored the adsorption mechanisms of counterions on the AuNP surface. The results demonstrated that stabilization is strongly influenced by the type of salt and storage conditions, with $NaNO_3$ increasing oxidation and NaCl and Na_2SO_3 improving size distribution and reducing aggregation. Light exposure negatively affected stability, whereas dark conditions promoted long-term suspension stability. Experimental findings were supported by DFT simulations, revealing strong counterion adsorption on the nanoparticle surface. These findings provide a critical understanding of the interactions governing nanoparticle stability, also offer practical solutions for extending the shelf life of AuNPs. This work paves the way for the development of more robust, contamination-free gold nanoparticles, promising significant advancements in biomedical, electronic, and catalytic applications.

Graphical Abstract

Keywords Gold nanoparticles · Laser ablation · Colloidal stability · Density functional theory (DFT) · Shelf-life extension

✉ Marcio Celso Fredel
m.fredel@ufsc.br

Philipi Cavalcante Ricardo
philipi.cavalcante@posgrad.ufsc.br

[1] Ceramic and Composite Materials Research Group (CERMAT), Mechanical Engineering Department, Federal University of Santa Catarina, Florianópolis, SC, Brazil

[2] Department of Chemistry, ampere – Laboratório de Plataformas Eletroquímicas, Federal University of Santa Catarina, Florianópolis, SC, Brazil

[3] Department of Physics, Federal University of Pelotas, Pelotas, Rio Grande do Sul, Brazil

[4] Center for MicroElectroMechanical Systems (CMEMS-UMinho), University of Minho, Guimarães, Portugal

[5] Centre for Textile Science and Technology (2C2T), University of Minho, Guimarães, Portugal

[6] Plasma and Radiation Physics, National Institute for Lasers, str. Atomistilor 409, Magurele 077125, Romania

Published online: 16 March 2026

1 Introduction

Gold nanoparticles (AuNPs) are among the most versatile and extensively studied nanomaterials due to their remarkable optical and electronic properties, enabling applications across catalysis [1], energy conversion [2], targeted drug and gene delivery [3, 4], sensing [5–7], and bioimaging [8]. Their appeal stems from their unique optical and electronic properties, particularly localized surface plasmon resonance (LSPR) [9], as well as their biocompatibility, tunable surface chemistry, and ease of functionalization [10]. Traditionally, AuNPs are synthesized by reducing gold tetrachloride ($HAuCl_4$) with chemical agents such as sodium citrate [11] or sodium borohydride [12, 13]. However, these conventional chemical methods often introduce residual contaminants, compromising nanoparticle purity, biocompatibility, and functionality.

Pulsed Laser Ablation in Liquid (PLAL) is a clean, reagent-free method for producing high-purity nanoparticles directly from bulk material, eliminating the need for ionic precursors and separation steps [14–16]. It allows control over morphology [17–19], well-defined sizes [7, 20], and high purity [21], though productivity and long-term stability remain challenges. Recent advances, including high-power, high-repetition-rate lasers, have boosted production to up to 4 g h^{-1} for metals such as gold, platinum, and silver [22, 23]. Techniques like multi-beam systems, high-speed scanners [24], and innovations such as wire targets or thin liquid layers have further improved efficiency, achieving up to fivefold increases without compromising nanoparticle quality [25].

Maintaining AuNPs colloidal stability is crucial for preserving their functionality, efficacy, and safety in biotechnological applications [26]. Aggregation can degrade nanoparticle performance and trigger adverse biological effects [27]. Stability and shelf life can be improved through appropriate stabilizers and optimized storage. Encapsulation with surfactants like CTAB [28], proteins like keratin and albumin [27], organic agents such as ω-sulfonylated alkylsulfanylaniline [29], or saline solutions containing sodium chloride [30] has proven effective. Additionally, proper purification and storage under controlled conditions are crucial for preserving the integrity of these nanoparticles [31].

The classical Derjaguin–Landau–Verwey–Overbeek (DLVO) theory explains colloidal stability through the balance between van der Waals attractions and electrostatic repulsions in ionic media [32, 33]. However, ligand-free AuNPs often exhibit behaviors beyond DLVO predictions, driven by ion-specific interactions in which particular anions and cations modulate surface charge and stability through selective adsorption and hydration effects [34–38]. For instance, ions such as Br^- and I^- enhance stabilization through adsorption-driven mechanisms [32, 34]. In saline media, nanoparticle stability arises from a complex interplay between ionic strength, ion valence, and hydration. Weakly hydrated anions promote stability, whereas strongly hydrated ones encourage aggregation, underscoring the role of ion hydration in colloidal behavior [34, 39–43]. Density functional theory (DFT) studies, though limited, support these findings by clarifying the energetics of ion adsorption on metallic surfaces [34, 44]. Nevertheless, the molecular-level mechanisms underlying colloidal stabilization of ligand-free AuNPs remain insufficiently understood. Classical models such as DLVO and Hofmeister series capture general trends but fail to explain the specific adsorption and hydration-driven effects that determine stability in the absence of organic ligands. This knowledge gap limits the rational design of stable, high-purity AuNPs for biological and catalytic applications.

To the best of our knowledge, a comprehensive understanding of AuNP stabilization in saline media, particularly regarding ion adsorption mechanisms and their correlation with colloidal behavior, remains incomplete. To address this, the present study investigates the stabilization of ligand-free AuNPs in saline environments by focusing on electrostatic and ion-specific adsorption mechanisms involving three representative salts: sodium chloride (NaCl), sodium nitrate ($NaNO_3$), and sodium sulfite (Na_2SO_3). These salts were deliberately chosen to encompass a spectrum of anionic properties and practical relevance. NaCl is a biologically compatible electrolyte widely present in physiological and industrial systems, serving as a reference for chloride's stabilizing behavior. $NaNO_3$, characterized by moderate hydration and weak adsorption, represents intermediate stabilization conditions, while Na_2SO_3, containing a divalent, strongly hydrated anion, is associated with destabilization phenomena. Collectively, these salts provide an effective framework for analyzing how ionic strength, valence, and hydration govern nanoparticle stability. Using a mixture design of experiments (DOE), the individual and combined effects of these salts on colloidal behavior were statistically assessed. Complementary DFT calculations elucidated the atomic-scale energetics of ion adsorption on gold surfaces. This integrated experimental–theoretical approach advances the understanding of stabilization dynamics in ligand-free AuNPs and supports the development of high-purity, contamination-resistant nanomaterials for biomedical and technological applications.

2 Materials And Methods

2.1 Materials

Sodium chloride (NaCl), sodium nitrate ($NaNO_3$), and sodium sulfite (Na_2SO_3) were purchased from Sigma-Aldrich and used without further purification. All salts were dissolved in freshly prepared ultrapure Milli-Q water (Millipore, ≤18.2 MΩ·cm) to obtain the respective saline solutions. The unbuffered solutions showed near-neutral pH values (6–8) depending on salt composition. No pH adjustment or degassing was performed, as all solutions were prepared and used under ambient laboratory conditions (22 ± 1 °C).

2.2 Preparation of Gold Suspension

Gold suspensions were synthesized by PLAL using a polished gold target (99.99% purity) with dimensions of 10 mm × 10 mm, immersed in 10 mL of a dilute electrolytic solution. A Nd: YAG laser (OEM Plus, Italy) operating at a wavelength of 1064 nm was used for ablation. The laser delivered an average output power of 6 W, a pulse width of 35 ns, and a repetition rate of 20 kHz. The beam was focused on the target surface using a fused-quartz lens with a 160 mm focal length, resulting in a 3 µm spot diameter. Under these conditions, the pulse energy was 0.3 mJ, and the corresponding laser fluence was calculated as 4.24 kJ·cm^{-2} per pulse [45].

The target was placed at the bottom of a borosilicate glass vessel, with the liquid level maintained 7 mm above its surface. Continuous magnetic stirring was applied during ablation to ensure homogeneous dispersion of the colloid and to prevent particle-induced shielding of the laser beam. The laser beam was scanned in a filled-rectangle pattern (4.5 mm × 2 mm) with a line spacing of 0.001 cm and a scan speed of 5 mm·s^{-1}, providing uniform irradiation and approximately twelve overlapping pulses per spot [14]. The ablation time was fixed at 11 min for all samples. This configuration ensured stable fluence, precise beam–target al.ignment, and reproducible synthesis conditions for all experiments.

Systems were produced under the following conditions: W (ultrapure water), Cl (100 µmol L^{-1} NaCl), N (100 µmol L^{-1} $NaNO_3$), S (100 µmol L^{-1} Na_2SO_3), ClN (50:50 µmol L^{-1} NaCl and $NaNO_3$), ClS (50:50 µmol L^{-1} NaCl and Na_2SO_3), NS (50:50 µmol L^{-1} $NaNO_3$ and Na_2SO_3), and ClNS (33:33:33 µmol L^{-1} NaCl, $NaNO_3$, and Na_2SO_3).

2.3 Characterization

2.3.1 UV – Vis Spectroscopy and Primary Particle Index (PPI)

UV–Vis spectra were collected in a Shimadzu UV − 1800 spectrophotometer (Shimadzu, Kyoto, Japan). The measurements were conducted in a 10 mm wide quartz cell with a sample volume of 2.0 mL, covering a spectral range from 300 to 800 nm.

The colloidal stability of the synthesized AuNPs was evaluated by calculating the PPI, defined as the ratio between the absorbance at 380 nm (interband transition of gold) and the scattering intensity at 800 nm [34], according to Eq. (1):

$$\mathrm{PPI} = \frac{A_{380}}{A_{800}} \tag{1}$$

where A_{380} and A_{800} represent the absorbance values at 380 nm and 800 nm, respectively. Higher PPI values indicate enhanced colloidal stability and lower aggregation levels [46].

2.3.2 Flame Atomic Absorption Spectroscopy (FAAS)

To quantify the gold concentration in the samples, the dispersions were first diluted with deionized water and subsequently mixed with 2 mL of aqua regia in a 10 mL volumetric flask. The gold content was then analyzed using a novAA 350 Flame Atomic Absorption Spectrometer (Analytik Jena, Germany). Measurements were performed in triplicate to ensure accuracy. The following conditions were employed: acetylene and argon as gases, a wavelength of 242.8 nm, slit width of 0.5 nm, lamp current of 4.0 mA, and an integration time of 3 s.

2.3.3 X-Ray Diffraction (XRD) Measurements

The Rigaku MiniFlex600 diffractometer 40 kV and 30 nA was used to conduct the X-ray diffraction (XRD) analyses to characterize the AuNPs crystallinity structure. The established parameters were a step of 0.05° and a scan speed of 10° min − 1 in a sweep 2θ range of 10–80 degrees. The samples were prepared by centrifuging aliquots of 100 µL each under a 6000-rpm machine for 20 min. Afterwards, 60 µL of the supernatant was removed and the concentrated AuNPs was dropped on a glass plate. The sample was taken to an oven under 30 °C until completely dry. This procedure was done 10 times to concentrate the samples for further analysis.

2.3.4 Zeta-Potential (ζ-potential) and Dynamic Light Scattering (DLS) Measurements

The zeta potential (ζ-potential) and dynamic light scattering (DLS) of the samples were measured using a Zetasizer Nano ZS equipped with a 4 mW He/Ne laser at 638 nm (Malvern, United Kingdom). A volume of 750 µL of each sample was placed in a disposable folded capillary cell for analysis. Zeta potential measurements were performed in triplicate ($n=3$), with 12 consecutive runs per replicate, to ensure reproducibility. Standard deviations derived from the triplicate datasets were calculated and employed as statistical error indicators. The DLS measurements were performed in triplicate ($n=3$) and taken at a fixed scattering angle of 173° and maintained at 25 °C, with water as the solvent.

2.3.5 High-Resolution Transmission Electron Microscopy (HRTEM)

HRTEM analyses were conducted using a Hitachi HD-2700 aberration-corrected STEM operated at 200 kV. Sample preparation involved placing 10 µL of the colloidal solutions onto carbon-coated copper grids, followed by air drying.

2.3.6 X-Ray Photoelectron Spectroscopy (XPS)

The chemical oxidation states of the gold nanoparticles were analyzed in detail using X-ray Photoelectron Spectroscopy (XPS). The samples were prepared by dropping 500 µL of the solution containing the Au NP onto a 5 × 5 mm Si substrate and placing the obtained samples into a forced convection oven slightly heated at 37 °C for a period of 24 h, to allow the evaporation of the liquid. The measurements were carried out with a K-Alpha Thermo Scientific (ESCALAB™ XI+, East Grinstead, UK) spectrometer, equipped with a 180° double-focusing hemispherical analyzer. Calibration was performed using the adventitious C1s peak at 284.8 eV for accurate charge referencing. Survey spectra were recorded at a pass energy of 50 eV to assess the surface elemental composition. High-resolution spectra for C1s, O1s, N1s, Na1s, Cl2p, S2p, and Au4f were recorded at a pass energy of 20 eV to provide a detailed analysis of the chemical oxidation states. The spectra acquisition and data processing were carried out using the Avantage software (Thermo Avantage v5 9921).

2.4 Molecular Dynamic Simulations

All calculations were conducted using the spin-polarized DFT [47, 48] within the generalized gradient approximation as proposed by Perdew-Burke-Ernzerhof (PBE) for the exchange-correlation functional [49]. To improve the accuracy in describing analyte-substrate interactions, especially where attractive non-local long-range van der Waals (vdW) interactions are significant, the semi-empirical vdW D3 correction [50, 51] was applied to all calculations. This correction adds additional dispersion energy contribution to the total DFT-PBE energy.

The Kohn-Sham equations were solved using the all-electron projected augmented wave (PAW) method [52, 53], as implemented in the Vienna Ab-initio Simulation Package (VASP) [54, 55]. Core electrons were described using fully relativistic calculations, while valence electrons were treated with a scalar-relativistic approximation [56, 57].

We utilized a plane-wave cutoff energy of 450 eV, which exceeds the largest recommended cutoff energy (ENMAX) among the selected PAW files by 12.5%. For model (*i*), a $3 \times 3 \times 1$ **k**-mesh was employed for Brillouin zone integration, generated using the Monkhorst-Pack scheme. In contrast, for models (*ii*) and (*iii*), a single **k**-point (**Γ**-point) was sufficient for all calculations, as there is no dispersion of electronic states along any direction within the Brillouin zone in these cases. Additionally, a small Gaussian smearing parameter of 1 meV was applied to prevent fractional occupation of electronic states.

Equilibrium geometries were considered achieved when the atomic forces on each atom were less than 0.015 eV/Å, with a total energy convergence criterion of 10^{-6} eV for electron density self-consistency. For ab initio molecular dynamics simulations, the Nosé algorithm was employed to control the temperature, with thermalization and simulated annealing processes running for approximately 20 and 40 picoseconds, respectively. A time step of 1 femtosecond was used to generate different adsorbed configuration snapshots, allowing for the exploration of various interaction configurations.

2.5 Design of Experiments and Statistical Analysis

The use of a simplex-centroid mixture design of experiments can offer several advantages in evaluating the colloidal stability of nanoparticles, including the identification of synergistic effects, optimization of compositions, quantitative assessment of interactions, predictive modelling, and versatility across different systems [58]. These advantages make this approach a valuable tool in the development and optimization of nanoparticle formulations.

Therefore, salt combinations were prepared according to the simplex-centroid mixture design with 2^{q-1} combinations, where q is the number of tested components (salts), with a sum equal to 1. Two repetitions of the central point (7 C) were included to allow for error calculation. The experimental domain consisted of components X1 (NaCl), X2 ($NaNO_3$), and X3 (Na_2SO_3), with each component

ranging between zero and one ($0 \leq Xi \leq 1$; $\sum Xi = 1$). The salt concentrations were randomly produced, where a value of 1.0 corresponds to 100 µM, 0.5 to 50 µM, and 0.3 to 33,33 µM, as detailed in Table 1. The resulting ionic strength of the systems is presented in Table S1 in the supporting information.

Mixture regression analysis was conducted to estimate the coefficients and assess the significance of the model terms using the F-test and the coefficient of determination (R^2). The analysis involved fitting the initial results to various mixture regression models, ranging from linear to special cubic, to determine the most appropriate model complexity. The significance of the model was evaluated based on several criteria: model significance, lack-of-fit significance, and adjusted R^2. The adjusted R^2 reflects the proportion of the variation in the responses explained by the model. The adjusted R^2 accounts for the number of terms in the model, providing a more accurate measure of fit by penalizing for excessive complexity.

Subsequently, the models were simplified by retaining only the significant terms, where applicable. The analysis determined that the most appropriate models were either linear, quadratic, or special cubic, depending on the specific context, based on criteria such as non-significant lack-of-fit and higher adjusted R^2 values. The models were defined as follows: Eq. (2) for the linear model, Eq. (3) for the quadratic model, and Eq. (4) for the special cubic model.

In this context, Y represents the predicted response from the analysis, while β_1, β_2, and β_3 denote the estimated coefficients for each linear effect term. Additionally, β_{12}, β_{13}, and β_{23} represent the coefficients for binary interaction effects, and β_{123} corresponds to the ternary interaction effect term. After deriving the estimated model equations, contour and surface plots were generated to visually illustrate the response to the three components specified in the model. Two new ternary mixtures were formulated to create distinct suspensions ($n = 2$). The model was then validated by comparing the mean responses of these suspensions with the values predicted by the model equations. The experimental design, data analysis, and generation of contour and surface plots were carried out in Statistica (TIBCO Software Inc., version 13.5.0.17, 2018), using a significance level of $\alpha = 0.05$.

Table 1 A simplex-centroid design with ratios of NaCl (X1), $NaNO_3$ (X2), and Na_2SO_3 (X3). The first three systems were labelled using the counterion corresponding to the salt content, i.e., NaCl = Cl, $NaNO_3$ = N, and Na_2SO_3 = S. In the other systems, the counterion of the corresponding salts was used to label the systems: ClN = mixture of NaCl and $NaNO_3$, ClS = mixture of NaCl and Na_2SO_3, NS = mixture of $NaNO_3$ and Na_2SO_3, and ClNS = mixture of NaCl, $NaNO_3$ and Na_2SO_3. W corresponds to the suspension produced only in ultrapure water

System	Salt Ratio ($*10^{-4}$ mol L^{-1})			Execution Order
	X1	X2	X3	
Cl	1.000	0.000	0.000	7 (C)
N	0.000	1.000	0.000	3
S	0.000	0.000	1.000	5
ClN	0.500	0.500	0.000	7 (C)
ClS	0.500	0.000	0.500	1
NS	0.000	0.500	0.500	4
ClNS (1)	0.333	0.333	0.333	2
ClNS (2)	0.333	0.333	0.333	7 (C)
ClNS (3)	0.333	0.333	0.333	6
W	0.000	0.000	0.000	0

3 Results and Discussion

This study investigates the effects of different salts (NaCl, $NaNO_3$, and Na_2SO_3) on the stabilization of gold nanoparticles produced by PLAL. We evaluate the decantation and aggregation processes over time under various storage conditions and analyse the molecular dynamics involved in physical adsorption processes. The systems were synthesized using a simplex-centroid mixture design of experiments, both with and without salts, and their combinations in ultrapure water.

UV-Vis spectroscopy was employed to assess the intrinsic optical properties of the synthesized AuNPs, FAAS quantified the productivity of the PLAL processes, while XRD analysis was performed to determine the crystalline structure of the AuNPs. To evaluate colloidal stability, we compared the ratio of gold interband absorbance at 380 nm to the scattering signal from aggregates and larger particles at 800 nm [34]. PPI serves as a critical metric for assessing the relative abundance of primary nanoparticles versus aggregates in a colloidal system [59]. Higher PPI values indicate improved colloidal stability, reduced aggregation, and enhanced nanoparticle dispersity, key factors for the performance of AuNPs in applications such as catalysis, sensing, and biomedical imaging [60].

Figure 1a illustrates that all systems exhibit a single absorbance peak corresponding to the LSPR phenomenon, with maxima ranging from 519 to 524 nm. Significant differences in absorbance are observed when comparing saline systems with the with ultrapure water (denoted as W) system. Notably, Na_2SO_3 (denoted as S) shows the highest absorbance, while the combination of NaCl and Na_2SO_3 (denoted as ClS) presents the lowest. As the LSPR phenomenon can offer an indication of the concentration of gold nanoparticle formation [61], these variations suggest complexities in productivity and nanoparticle formation, which may be influenced by the direct effect of ion type on the electrostatic interaction between the forming nanoparticles and water [40, 62].

Figure 1b presents the PPI values of different systems, showing higher stability in the system with NaCl (denoted as Cl) and its mixtures with $NaNO_3$ and Na_2SO_3 (denoted as ClNS). In contrast, systems with ultrapure water (denoted as W) and $NaNO_3$ (denoted as N) exhibited the lowest PPI values, indicating poorer colloidal stability and a higher tendency for aggregation. The enhanced PPI values in NaCl-containing systems can be attributed to adsorption processes and electrostatic interactions on the nanomaterial surface, which suppress aggregation and improve colloidal stability [46]. Similarly, systems containing Na_2SO_3 showed an increase in PPI, likely due to complex sulfur adsorption and interaction processes on the surface of the AuNPs [63].

The outcomes suggest that the type of salt used significantly influences the productivity (mg h^{-1}) of the synthesized nanomaterial. As shown in Fig. 1c,the productivity values, determined by FAAS, vary depending on the salt present during the PLAL process. The presence of Cl and S salts during the synthesis appears to enhance the ablation process, leading to higher productivity of AuNPs. In contrast, N salts seem to have a neutral impact on AuNPs generation when compared to system W. It shows that while individual salts and the triple salt mixture (CINS) positively affect productivity, combinations of two salts tend to reduce the efficiency of the PLAL technique. The addition of salts to the aqueous medium during laser ablation likely increases the material removal rate. This enhancement could be linked to the increased energy density of the laser-induced plasma. Fully dissociated ions in the solution may reduce the effective ionization energy, lowering the intensity threshold for plasma generation and increasing the charge density within the breakdown region [64]. These effects collectively contribute to the observed improvements in productivity.

Figure 1presents the diffractograms obtained through XRD analysis of dried samples, where characteristic peaks of gold are observed at 38.2°, 44.4°, 64.6°, and 77.7°. These peaks can be indexed to the (111), (200), (220), and (311) diffraction planes of the face-centered cubic (FCC) structure of metallic gold, respectively, indicating that the synthesized gold nanoparticles consist of pure crystalline gold.

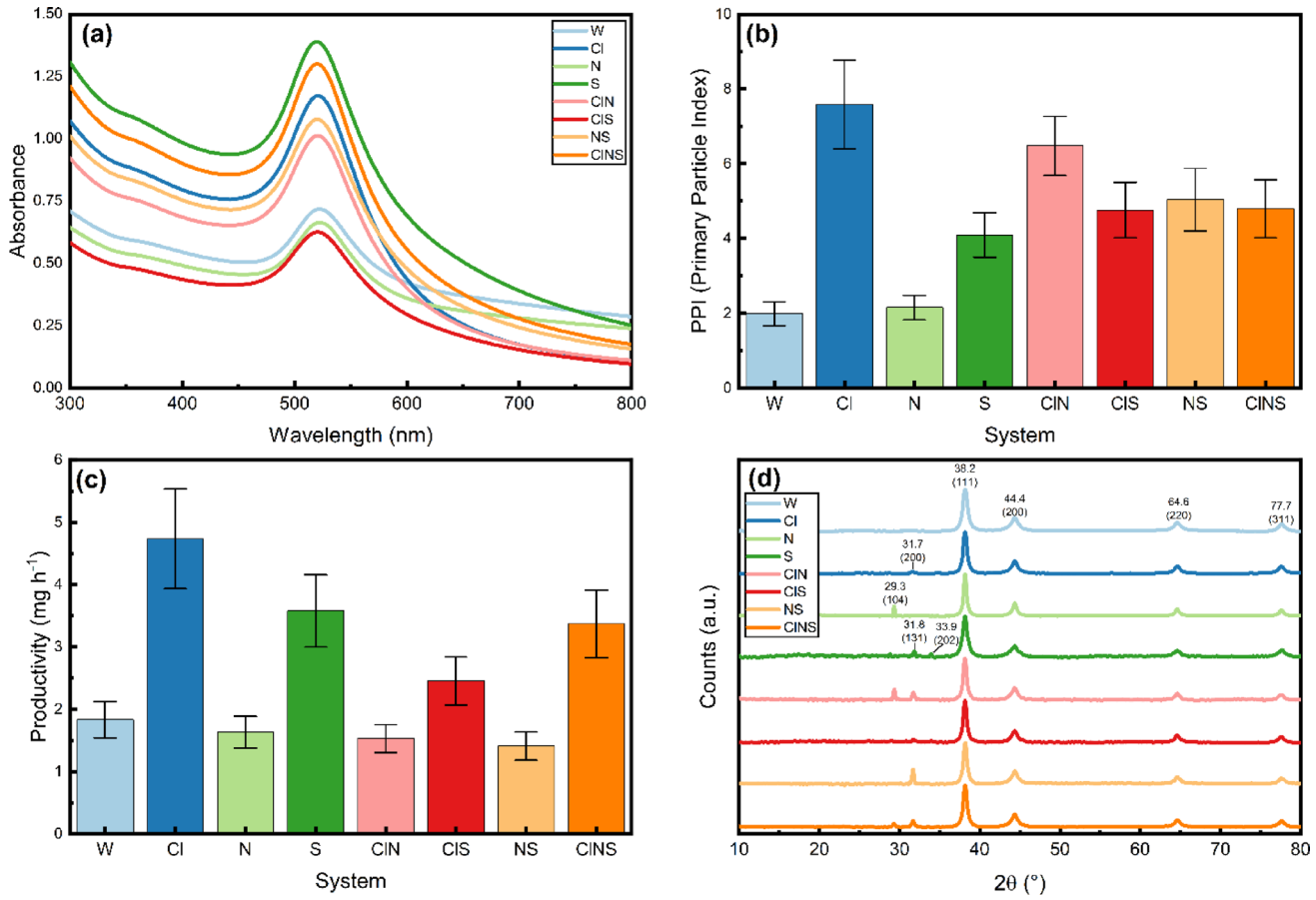

Fig. 1 Optical and productivity analysis of gold nanoparticles synthesized under various conditions. (**a**) UV-Vis absorbance spectra showing LSPR for each system after PLAL production. (**b**) PPI, calculated as the ratio of absorbance at 380 nm to the scattering signal at 800 nm (A380/A800), indicating colloidal stability and **(c)** Productivity of AuNPs as determined by FAAS. (**d**) XRD diffractograms illustrating the diffraction peaks of AuNPs and the associated salts, with detailed indexing of the corresponding Miller indices (hkl). Data represent the mean of three independent experiments (n = 3). Error bars indicate the standard deviation (SD)

The peak corresponding to the (111) plane is notably more intense than those of the other planes, suggesting a predominant (111) orientation and confirming the crystalline nature of the gold nanoparticles [46].

In systems containing salts, the corresponding characteristic peaks are observed in the diffractograms, as expected. These peaks are attributed to the crystalline forms of NaCl, $NaNO_3$, and Na_2SO_4, present in the dried samples of salt suspensions. In the chloride-containing system, a distinct peak is observed at 31.7°, corresponding to the (200) diffraction planes of the face-centered cubic structure of crystallized NaCl [65]. In the nitrate-containing system, a slightly more intense peak at 29.3° corresponds to the (104) diffraction planes of the rhombohedral structure of $NaNO_3$ [66]. For the sulfite system, two distinct peaks are observed at 31.8° and 33.9°, corresponding to Na_2SO_4 rather than Na_2SO_3 as initially anticipated. Literature suggests that Na_2SO_3 may easily oxidize to Na_2SO_4 [67]. Furthermore, the presence of gold nanoparticles, which act as catalytic agents, enhances the conditions for oxidation [68].

In the mixed systems, the characteristic nitrate peak is observed in both the ClN and ClNS systems, as anticipated. However, in systems containing sulfate, only a single peak at 31.8° is present, as observed in both the NS and ClNS systems, with the second peak at 33.9° notably absent. In the ClS system, the peaks for chloride and sulfate are nearly indistinguishable due to their discrete characteristics. Notably, in all gold nanoparticle-containing systems, while salt peaks are observed, no new crystalline angles for the gold nanoparticles are detected. Therefore, the nanoparticles consistently exhibit the face-centered cubic structure, even when subjected to synthesis under saline conditions. This indicates that no lattice distortion or structural modification of the gold nanoparticles occurred as a result of oxidation processes, confirming that the gold remained in its metallic FCC form under all tested conditions.

Zeta (ζ)-potential analysis is a commonly used technique for characterizing nanoparticles, as it provides crucial information about the electrostatic potential at the slipping plane of a particle concerning the electric double layer (EDL) surrounding it and its dispersant [69]. Typically, ζ-potential values between ±30 and ±40 mV indicate moderate electrostatic stability, while values exceeding ±40 mV suggest strong electrostatic stability [70].

In the present work, ζ-potential values were measured both immediately after synthesis and 90 days later for samples stored in a refrigerated (4–8 °C) environment and sonicated before analysis. As shown in Fig. 2, all AuNPs stabilized with salts exhibited at least moderate electrostatic stability. In contrast, the AuNPs synthesized in ultrapure water showed colloidal instability, with a ζ-potential of −25.77 mV. Notably, the samples containing sodium sulfite demonstrated the most significant stabilization, with the best ζ-potential value recorded at −51.23 mV. This enhanced stability can be attributed to the presence of SO_3^{2-} on the surface of the AuNPs, with the sulfite's total charge (−2) responsible for the higher surface charge density around the nanoparticles [71]. Thus, this situation leads to a more negative ζ-potential, providing a robust electrostatic stabilization and leading the AuNPs synthesized with Na_2SO_3 a particularly effective stabilizing agent in this context.

After 90 days, the AuNP synthesized in the presence of salts exhibited a decrease in ζ-potential values, indicating a loss of stability. Among these, the samples containing SO_3^{2-} showed a relatively smaller decrease in ζ-potential, which can be attributed to the strong Au-S interaction as previously mentioned. Generally, laser-ablated AuNPs in halide water media change particle chemical composition and gold surface oxidation due to ionic contributions [40]. Similarly, it can be inferred that the differences between the anions in the various salts result in strong or weak interactions, accounting for the observed reduction in ζ-potential over time. This will be further explored in the subsequent computational simulations. The application of statistical mixture models for UV-Vis, PPI and Zeta Potential analyses are presented in the **Supporting Information**.

HRTEM was used to examine the morphology and size distribution of AuNPs synthesized in different saline environments (Fig. 3a–h). Across all systems, particles exhibited predominantly spherical shapes with log-normal size distributions, as indicated by right-skewed histograms, suggesting secondary growth or partial aggregation during synthesis. Nanoparticles produced in pure water (W) and nitrate medium (N) displayed the largest mean diameters (D_{Mean} = 14.6 nm and 24.8 nm, respectively) and visible clustering. These observations align with the lower plasmon peak intensities (PPI) in UV–Vis spectra, confirming weaker colloidal stabilization and enhanced aggregation [34, 46]. The larger sizes in these systems likely result from slower nucleation and increased coalescence during laser ablation, yielding broader size distributions.

In contrast, mixed-salt environments (Fig. 3b–h) yielded smaller mean diameters and reduced aggregation, indicating improved growth control. Among single-salt systems, the sulfite sample (S) formed nanoparticles averaging 9.3 nm, while in ClS, NS, and ClNS systems, mean diameters decreased further to 6.8, 6.1, and 8.4 nm, respectively. These results emphasize the strong stabilizing role of SO_3^{2-} anions, which act as Lewis bases forming π back-bonding and electrostatic interactions with gold surfaces [72]. Such interactions promote compact, well-stabilized nanoparticles and inhibit uncontrolled aggregation.

The combination of sulfite with other anions (e.g., Cl^- or NO_3^-) produced smaller, more uniform particles, suggesting

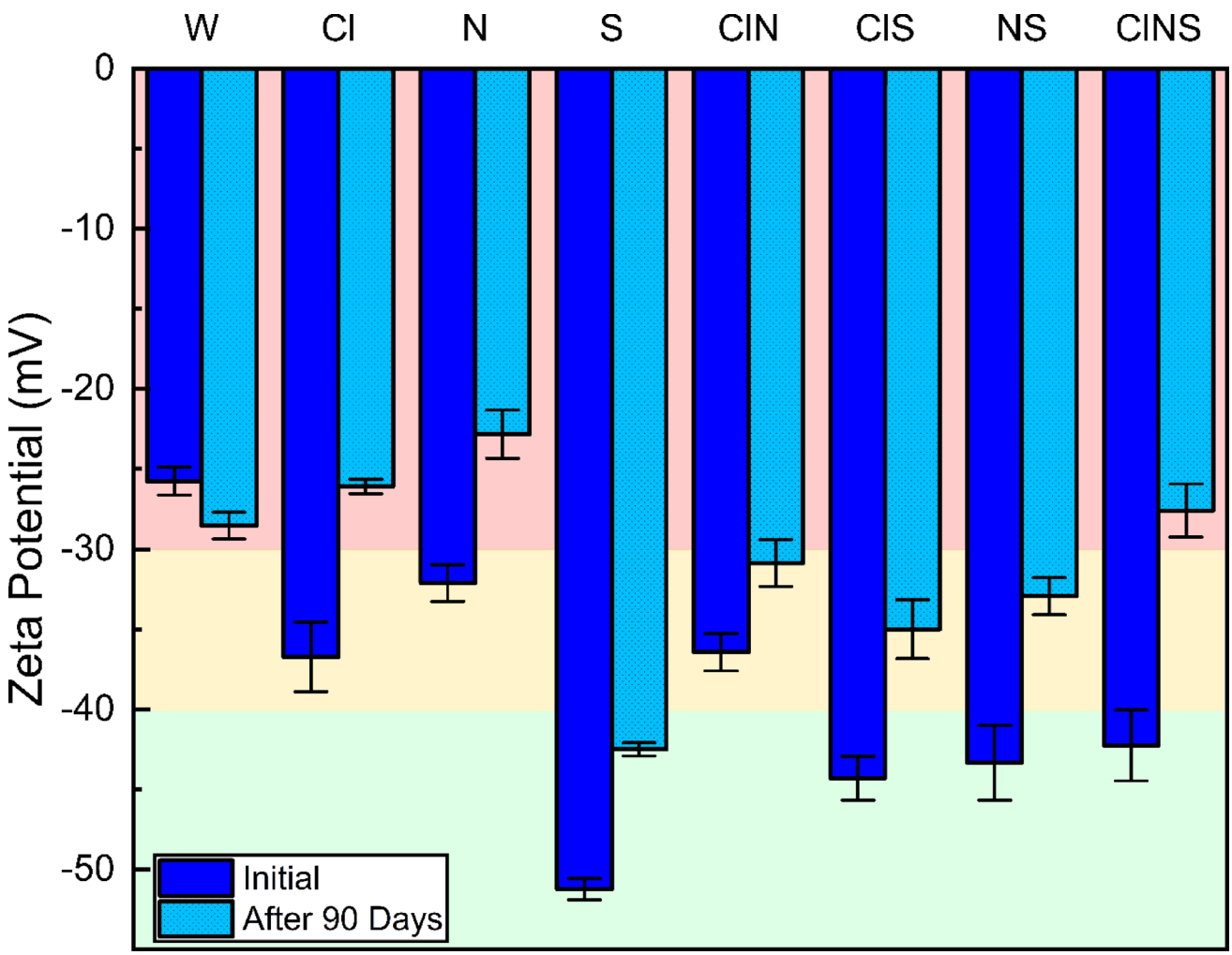

Fig. 2 ζ-potential values for different AuNP systems, measured on the day after synthesis and after 90 days. Data represent the mean of three independent experiments ($n = 3$). Error bars indicate the standard deviation (SD)

a synergistic stabilization effect. This synergy likely stems from differential adsorption affinities: SO_3^{2-} provides charge stabilization through strong surface binding, whereas Cl^- and NO_3^- modulate surface potential and ionic strength. These findings are consistent with previous reports showing that NO_3^- and Cl^- afford intermediate stabilization, while SO_3^{2-} confers stronger coordination, leading to monodisperse colloids [34].

DLS further elucidated colloidal behavior across systems (Fig. 4a–h). Each exhibited multiple scattering populations, indicating variable degrees of aggregation and stabilization in solution [62]. The Cl and S systems showed the smallest hydrodynamic diameters, with dominant peaks at 32.7 nm (4.95%) and 28.2 nm (4.3%), respectively. Their low hydrodynamic sizes and moderate intensities indicate efficient stabilization and minimal aggregation [73, 74]. Minor populations at 2.33 nm and 5.61 nm in Cl likely correspond to primary clusters or ionic species. Conversely, N and W systems exhibited broader distributions and pronounced aggregation. The N system contained populations at 11.7 nm (1.97%), 78.8 nm (12.7%), and 5560 nm (1.1%), reflecting both nanoscale species and secondary aggregates. Similarly, the W control showed a dominant peak at 78.8 nm (10.33%) and a large secondary peak at 5550 nm (1.1%), confirming extensive aggregation without ionic stabilization [75].

Mixed-ion systems displayed more complex distributions. The ClN system exhibited peaks at 50.7 nm (6.72%) and 255 nm (7.92%), indicating moderately stabilized yet partially aggregated nanoparticles. The ClS system presented three peaks, 43.8 nm (6.71%), 220 nm (5.46%), and 5560 nm (1.35%), suggesting partial aggregation due to competitive adsorption between Cl^- and sulfur species. Similarly, NS showed peaks at 43.8 nm (5.98%), 164 nm (5.09%), and 5560 nm (2.3%), reflecting bimodal stabilization with some aggregation. The ClNS system exhibited a broad, polydisperse profile with peaks at 1.29 nm (0.49%), 5.61 nm (0.56%), 68.1 nm (5.69%), and 4800 nm (0.34%), suggesting coexistence of small stabilized clusters and

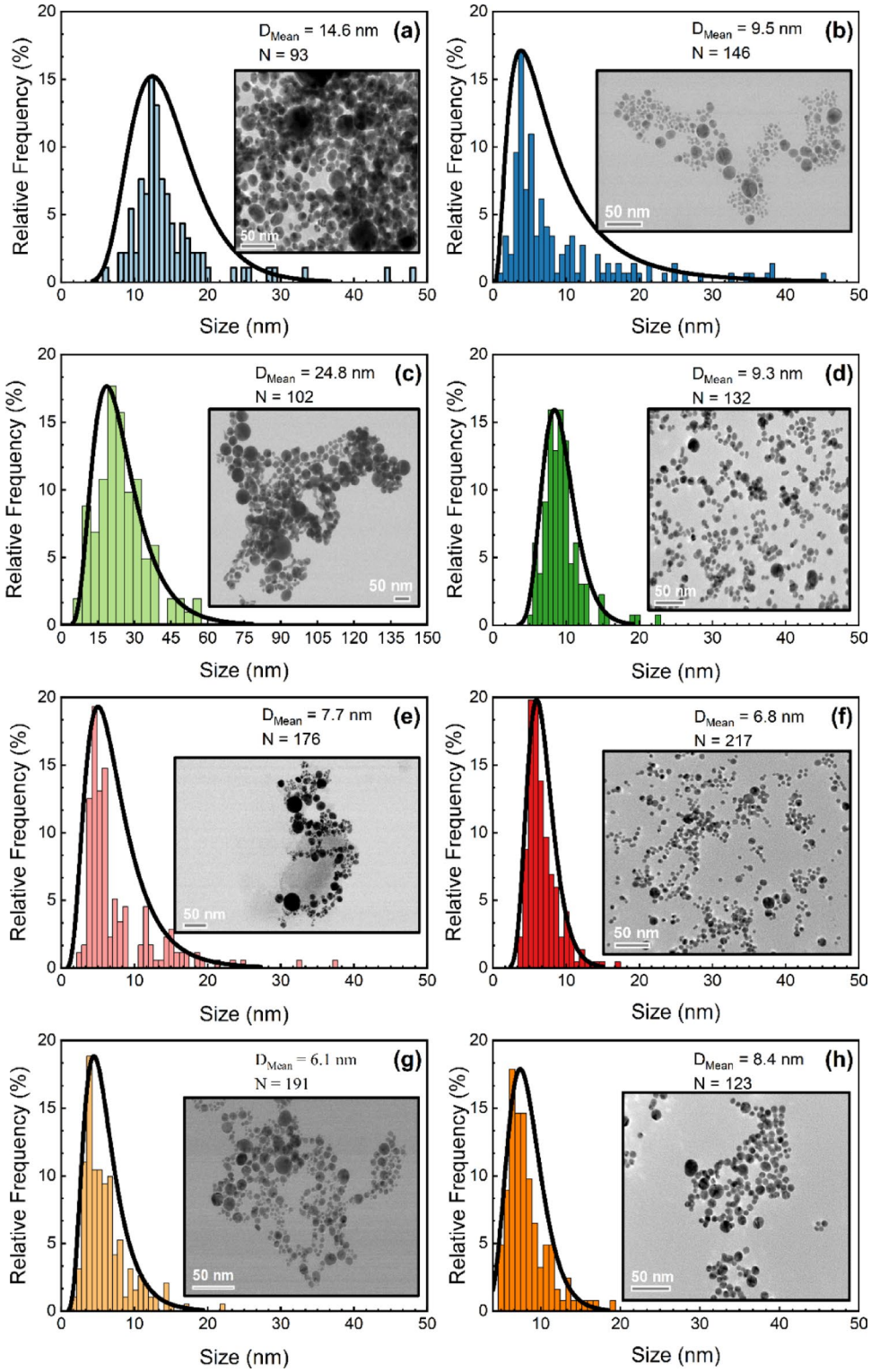

Fig. 3 Size distribution histograms of HRTEM micrographs of AuNPs (*inset*) synthesized in (**a**) W, (**b**) Cl, (**c**) N, (**d**) S, (**e**) ClN, (**f**) ClS, (**g**) NS and (**h**) ClNS

large aggregates [76]. The presence of sub-10 nm species may correspond to ligand-stabilized nuclei coexisting with larger colloids [73, 76]. Overall, the dominant particle size increased in the order: Cl≈S<NS<ClN≈ClS<ClNS<N<W.

After 90 days, DLS analysis revealed clear shifts in hydrodynamic size distributions across all systems, highlighting the progressive evolution of colloidal stability. The W control maintained its triphasic distribution, with peaks at 8.72 nm (1.76%), 78.8 nm (9.01%), and 5560 nm

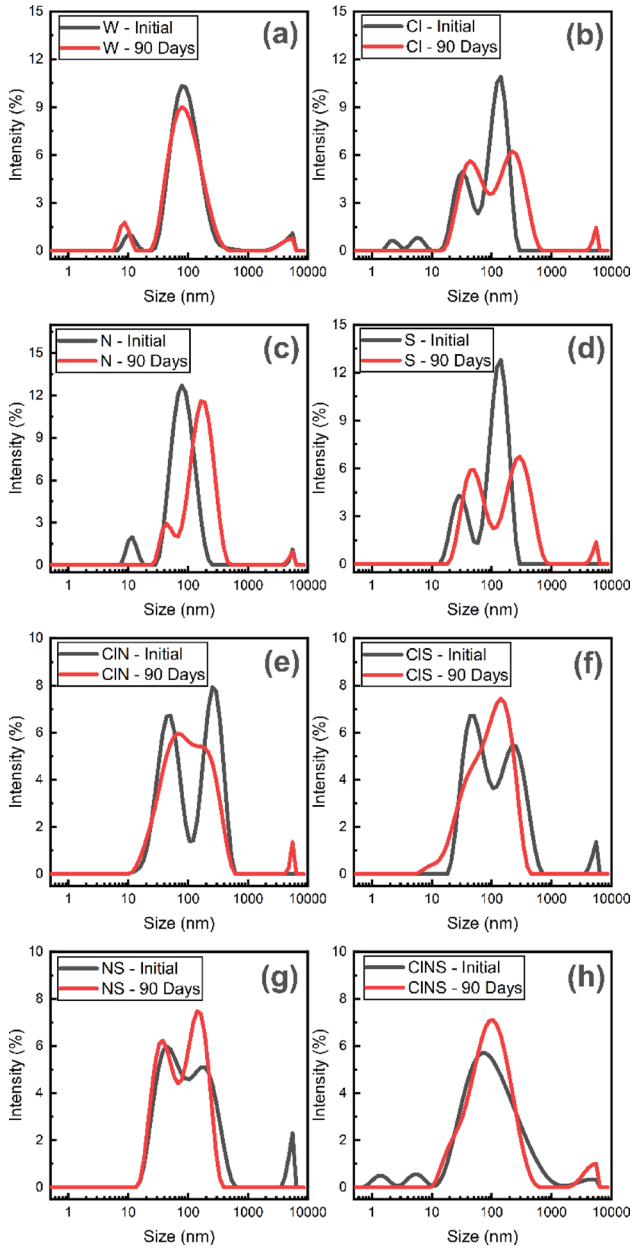

Fig. 4 Size distribution histograms of DLS measurements of AuNPs, measured on the day after synthesis (black line) and after 90 days (red line), (*inset*) synthesized in (**a**) W, (**b**) Cl, (**c**) N, (**d**) S, (**e**) ClN, (**f**) ClS, (**g**) NS and (**h**) ClNS. Data represent the mean of three independent experiments ($n=3$)

(0.76%), indicating persistent aggregation and limited stability over time [75]. The Cl system remained comparatively stable, with peaks shifting to 43.8 nm (5.62%), 220 nm (6.22%), and 5560 nm (1.45%), suggesting modest growth and slight aggregation likely driven by gradual surface ion rearrangement [74]. The N system, however, exhibited enhanced aggregation, now characterized by peaks at 43.8 nm (2.91%), 164 nm (11.6%), and 5560 nm (0.95%). The pronounced intensity at 164 nm indicates the formation of secondary aggregates, consistent with insufficient electrostatic stabilization in nitrogen-only media [75].

The S system evolved toward larger hydrodynamic sizes, with peaks at 50.7 nm (5.89%), 295 nm (6.73%), and 5560 nm (1.37%), suggesting progressive particle growth. This behavior likely reflects slow oxidation or reorganization of sulfur species at the surface, leading to partial loss of stabilization [77]. Among the mixed-ion systems, the ClN sample showed peaks at 68.1 nm (5.96%), 190 nm (5.35%), and 5560 nm (1.34%), indicating moderate aggregation and narrowing of the initial bimodal distribution. The ClS system displayed a single dominant peak at 142 nm (7.44%), implying that smaller particles had coalesced into larger, yet stable secondary aggregates. Similarly, the NS system presented two main populations at 37.88 nm (6.23%) and 142 nm (7.48%), suggesting that a fraction of small colloids remained stable while larger assemblies grew over time. The ClNS system, initially highly polydisperse, evolved into a single dominant peak at 106 nm (7.1%), indicating aggregation-driven coarsening but stabilization of the resulting larger colloids. The disappearance of sub-10 nm species suggests a transition from ligand-stabilized clusters to thermodynamically stable aggregates governed by multi-ion surface coordination.

The evaluation of the DLS data before and after aging revealed that the hierarchy of dominant particle sizes after 90 days followed the order Cl≈S<ClN<NS<ClS<ClNS<N<W. The chloride- and sulfur-based systems exhibited the smallest particle sizes and least aggregation, confirming their superior stabilizing capacity, likely due to persistent electrostatic and specific adsorption effects [74]. In contrast, nitrogen-only and control systems experienced significant aggregation, consistent with weaker surface interactions and insufficient ionic shielding [75]. Mixed-ion systems achieved intermediate stability, with the ClNS system demonstrating a transition toward kinetically and thermodynamically stable aggregates [76].

Comparison of DLS and HRTEM results reveals systematic size discrepancies, reflecting the distinct measurement principles of each technique. DLS determines the hydrodynamic diameter, which includes the gold core, solvation shell, and adsorbed ions or ligands, whereas HRTEM measures the dry-state core, excluding hydration and loosely bound species [78]. For example, DLS identified dominant peaks near 28–33 nm for Cl and S systems, while HRTEM (Fig. 3a–h) showed smaller cores of 5–20 nm, consistent with PLAL-synthesized AuNPs. The larger DLS values arise from hydrated coronas influenced by ionic strength, surface charge, and adsorbed salts [69]. Beyond these general electrostatic factors, ion-specific interactions also contribute to modulating the hydration shell, with kosmotropic anions (e.g., sulfite or sulfate in S) enhancing water

structuring and increasing hydrodynamic radii, whereas chaotropic ions (e.g., chloride in Cl) weaken hydration layers, slightly reducing apparent size [79]. The W control's DLS peak at 5.6 µm indicates macroscopic aggregation, while broad distributions in mixed-ion systems (e.g., ClNS) reflect heterogeneous ion adsorption that perturbs surface charge and colloidal stability.

The collective interpretation of ζ-potential, HRTEM, and DLS analyses establishes a clear relationship between surface charge, nanoparticle morphology, and colloidal behavior. Systems exhibiting higher absolute ζ-potential values, particularly those containing sulfite, produced smaller and more uniform gold cores, coupled with reduced hydrodynamic diameters and minimal aggregation [80]. These observations confirm that strong electrostatic repulsion and specific Au–S interactions govern both the initial nucleation process and the long-term stability of the colloids [81]. Mixed-ion systems displayed intermediate stability, reflecting the balance between competitive anion adsorption and partial charge neutralization, whereas nitrate and pure-water systems remained prone to aggregation due to insufficient electrostatic and chemical stabilization [39, 75].

Given that electrostatic stabilization is intimately linked to surface chemistry, a deeper understanding of the oxidation state and surface electronic structure of the AuNPs is essential [82]. To elucidate how different ionic environments influence surface composition and stabilization mechanisms, XPS was used to analyze the oxidation states of nanoparticles synthesized in both ultrapure water and a saline system [83]. The resulting spectra, shown in Fig. 5a-d, confirm the presence of two stable oxidation states, Au^{1+} and Au^{3+}. These states are observed both in the absence of salts, as in the W system (Fig. 5a), and in saline media, such as the N system, which displays a prominent band at 84.57 eV corresponding to Au^{1+} (Fig. 5c). Similar spectra for other samples are provided in the Supplementary Information (**Figure S1a-d**).

The Au 4f peak predominantly appears around 85 eV. In our systems, the dominant features corresponding to the $4f_{7/2}$ (around 83 eV) and $4f_{5/2}$ (around 87 eV) peaks of elemental gold were observed separated by the Au 4f spin-orbit-splitting of ~3.67 eV. In Fig. 5a, system W exhibits approximately 6.4% of its surface atoms in an oxidized state. Figure 5b presents the Cl system, where 6.8% of the

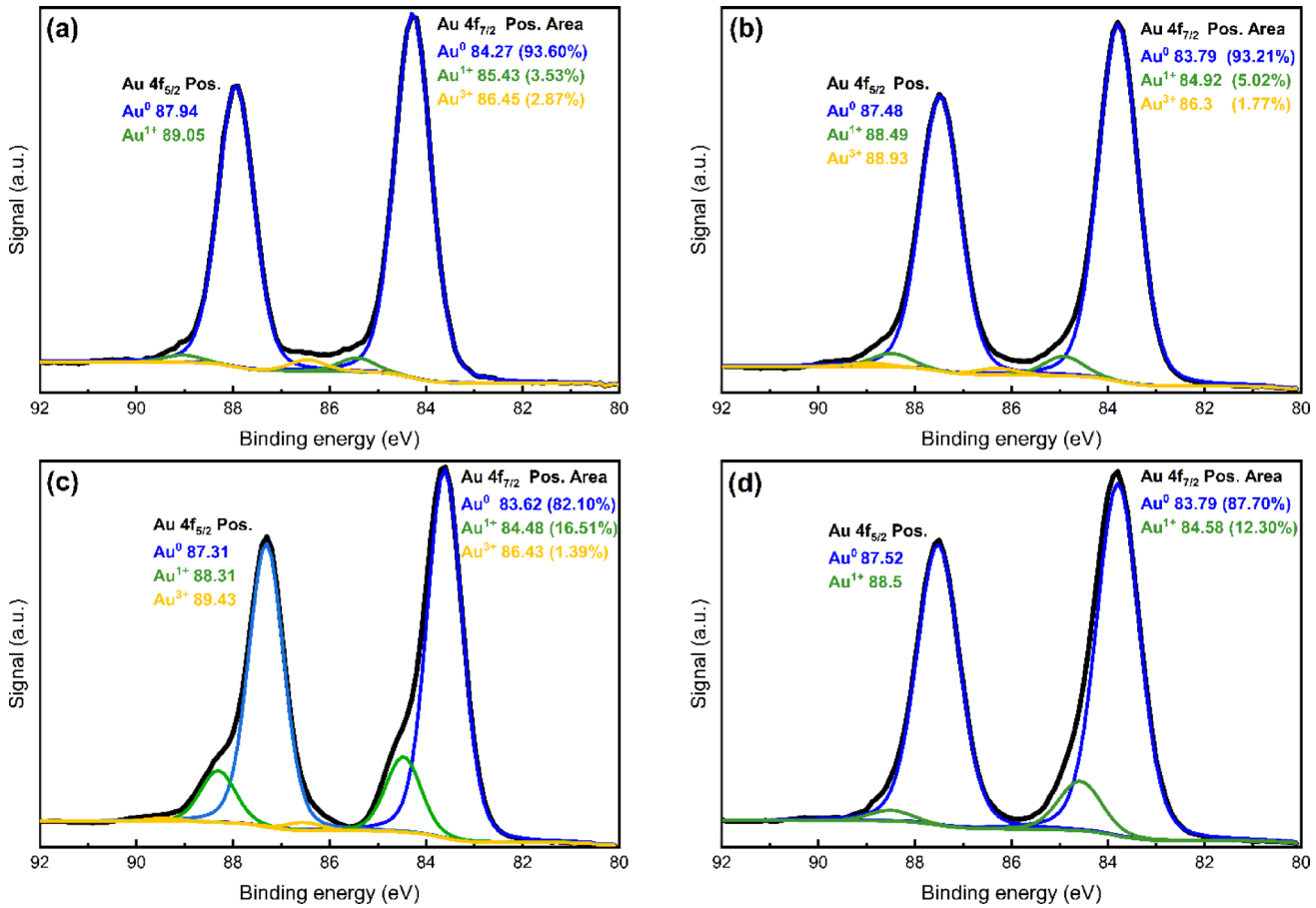

Fig. 5 XPS spectra of AuNPs generated under (**a**) salt-free conditions (W), (**b**) saline conditions with 100 µmol L^{-1} NaCl, (**c**) 100 µmol L^{-1} $NaNO_3$, and (**d**) 100 µmol L^{-1} Na_2SO_3

surface atoms are oxidized. Figure 5c shows the N system with 17.9% of its surface atoms in an oxidized state, while Fig. 5d illustrates system S, which has approximately 12.3% of its surface atoms in an oxidized state.

For the AuNPs synthesized in $NaNO_3$, the oxidized Au^{1+} species account for 16.50% of the signal, while 1.39% arises from Au^{3+} findings. This suggests that the NO_3^- counter-ion can promote a higher oxidation state on the surface of AuNPs, especially during the PLAL process. As observed by Letzel et al., (2017) [84], salts act in the vapour phase of the cavitation bubble and interact electrostatically with the nanoparticle surface, which may explain the increase in oxidized species caused by the NO_3^- counter-ion. For AuNPs synthesized in Na_2SO_3 (Fig. 5d), surface oxidation is notably lower in comparison to system N, with Au^{1+} at 12.3%. showing only one state of oxidation. This observation is consistent across mixed systems ClN, ClS, NS, and ClNS, as shown in **Figure S1a-d**.

Quantitatively, the XPS results reveal that AuNPs synthesized in $NaNO_3$ exhibit 17.9% of oxidized surface atoms, comprising 16.5% Au^+ and 1.4% Au^{3+} species. This oxidation level is nearly three times higher than that observed in NaCl (6.8%) and ultrapure water (6.4%), confirming the oxidative influence of nitrate ions during laser ablation. Conversely, Na_2SO_3 reduced the oxidation extent to 12.3%, while mixed chloride–sulfite systems (ClS) showed no detectable oxidized species, evidencing a synergistic passivation effect. These quantitative trends align with morphological analyses, in which NaCl- and Na_2SO_3-containing systems produced smaller and more uniform nanoparticles (6.8–9.3 nm) than $NaNO_3$ or water-based samples (14.6–24.8 nm). Together, these findings substantiate that nitrate enhances surface oxidation, whereas chloride and sulfite improve nanoparticle size distribution and stabilization through distinct electrostatic and coordination-driven mechanisms.

This finding is supported by theoretical analyses presented in the next section, which suggest that the SO_3^{2-} counter-ion exerts a stronger influence compared to chlorine and nitrogen counter-ions. The sulfur atom complex more effectively to the gold surface, leading to a reduction in the oxidation state of the nanoparticles.

Figure S1b presents an intriguing result from the XPS spectra of AuNPs synthesized in the chloride-sulfite (ClS) mixed system, revealing the absence of oxidation. This phenomenon may arise from the combined interactions of chloride (Cl^-) and sulfite (SO_3^{2-}) ions with the AuNP surface. Sulfite ions likely contribute to surface passivation through coordinate bonding with gold, potentially forming a barrier that reduces the availability of active sites and limits access to oxidative species. Chloride ions may provide additional stabilization through electrostatic interactions, complementing the passivating effect of sulfite. These interactions together may create a stabilized surface environment that minimizes oxidation.

A comparison between AuNPs synthesized via chemical reduction with citrate and those obtained through PLAL reveals significant advantages for the latter in terms of purity, colloidal stability, size distribution, and zeta potential. Citrate-capped AuNPs exhibit moderate stability, typically characterized by zeta potential values around −37 mV and hydrodynamic diameters near 21.6 nm. Although they can remain dispersed under mild conditions (e.g., temperatures up to 70 °C and ionic strengths up to 100 mM NaCl), their stabilization relies on weak electrostatic adsorption of citrate anions to the nanoparticle surface [85]. This non-covalent interaction is sensitive to ionic competition and electric double-layer compression, often resulting in aggregation over time. In contrast, PLAL-produced AuNPs synthesized in saline media such as NaCl and Na_2SO_3 not only exhibit smaller sizes and narrower distributions (average diameters ranging from 6.1 to 9.3 nm), but also show more negative zeta potentials (up to −51.23 mV), indicating stronger electrostatic repulsion and significantly higher colloidal stability, maintained even after 90 days of storage. Importantly, these nanoparticles are synthesized without any ligands or surfactants, which eliminates the risk of contamination, preserves colloidal purity, and facilitates direct transfer to biological media such as RPMI, FBS, and TRIS buffer [26]. This ligand-free system, stabilized solely by ion adsorption and electrostatic interactions, represents a promising platform for biomedical, catalytic, and sensing applications where long-term stability and material purity are essential.

In summary, this study underscores the critical influence of saline media on the surface oxidation states and stabilization dynamics of AuNPs synthesized via PLAL. XPS analyses revealed that different counter-ions significantly affect the oxidation and stabilization of AuNPs. While nitrate (NO_3^-) ions promoted higher oxidation states, sulfite (SO_3^{2-}) ions demonstrated a pronounced ability to reduce oxidation, likely through the formation of stable, passivating surface layers. In mixed systems, such as chloride-sulfite (ClS), synergistic effects led to complete suppression of oxidation, emphasizing the role of ionic interactions in shaping nanoparticle surface properties. These findings not only provide valuable insights into the role of ion-specific interactions in modulating the surface chemistry of AuNPs but also highlight the necessity for advanced analytical methods, such as Core-Level Bayesian Fitting, to enhance the accuracy of oxidation state measurements.

4 Computational Modelling

Computational simulations were used to investigate the contributions of electrostatic interactions and potential salt adsorption on the surface of AuNPs. High-level quantum-mechanical calculations based on density functional theory (DFT) were employed to elucidate the stabilization mechanisms during the synthesis of AuNPs using various salts: NaCl, $NaNO_3$, and Na_2SO_3. In line with the experimental synthesis process, which facilitates the interaction of salt molecules with the surface of AuNPs, our modelling approach focused on three distinct chemical environments frequently encountered during molecular adsorption processes on AuNPs surfaces, which were optimized through in-depth analyses.

To achieve this goal, the analysis of chemical environments considered different interaction scenarios involving molecules and distinct coordination and reactivity environments in AuNPs. Specifically, we explored situations such as (*i*) interaction with a highly coordinated pristine Au surface (effective coordination number, ECN = 9), namely Au (111) surface, which was modelled using a close-packed Au slab. This surface is derived from the face-centered cubic (fcc) crystal lattice, produced by cleaving the Au bulk fcc (ECN = 12) along the [111] direction. Notably, the Au (111) surface is recognized as one of the most stable configurations of Au [86]. Consequently, it plays a critical role as a coating form for AuNPs, offering various adsorption possibilities through top (one-fold), bridge (two-fold), and hollow (three-fold) sites.

Furthermore, we considered chemical interaction environments where molecules encounter regions of low coordination on the surface of AuNPs. These low-coordination regions can arise during synthesis due to structural flaws, the defect's presence, or the aggregation of Au atoms into atomic clusters. To effectively model these scenarios, we employed subnanometer and nanometer-sized clusters. In addition to the highly coordinated pristine Au surface (*i*), we introduced two additional models to represent environments with lower coordination and higher reactivity. (*ii*) The first of these models involved atomic systems ranging from 1 to 2 nm, specifically Au nanoclusters consisting of 55 atoms (Au_{55}, ~ 1.4 nm) [87, 88]. This model enabled us to expose molecules to regions such as edges (ECN = 8.0) and corners (ECN = 6.0).

In the most reduced and minute case (*iii*), we considered atomic systems with a size of < 1 nm, utilizing the model of Au subnanoclusters consisting of 13 atoms, (Au_{13}, ~ 0.8 nm) [87]. This model allowed for the exposure of molecules to sites with even lower coordination, such as ECN = 6.0, providing access to more reactive regions due to the cluster's finite atomic structure, characterized by a minimal number of first neighbours. The last two models, involving nanoclusters and subnanoclusters, exhibit a diverse array of adsorption sites, including 1-, 2-, and 3- or 4-fold coordination sites. Therefore, the models (*i*) to (*iii*) collectively encompass a wide range of potential chemical interaction environments within AuNPs at an atomistic level.

Utilizing the hard sphere model, the constituent subsystems of the adopted models feature atoms exposed to the vacuum (or any external chemical environment), termed surface atoms, while atoms not directly exposed to the vacuum region are referred to as core atoms. All three models exhibit compact structures with high coordination, a fundamental trait of metallic systems. Except for case (*i*), which comprises an Au slab model, the 13 and 55 atom models are based on the compact geometry that most closely resembles a spherical particle at these scales, specifically, the icosahedron (ICO) structure, corresponding to the I_h space group [88]. The ICO structure features fivefold rotational symmetry axes, and its surfaces are exclusively composed of (111)-like close-packed facets.

The specific numbers of atoms selected for the subnanocluster and nanocluster models, namely 13 and 55 atoms, respectively, correspond to the initial two numbers in the sequence of atomic layer closure models. These numbers represent compact structures comprising complete atomic layers, where 13 = 1 + 12 and 55 = 1 + 12 + 42, respectively [89]. In the Au_{13} model, there are two non-equivalent atoms: the central (internal) atom, which has a coordination number of 12.0, and the 12 peripheral atoms, each with a coordination number of 6.0. These external atoms are equidistant from the central atom, forming a highly symmetric structure.

In the Au_{55} model, five nonequivalent atoms are distributed across three atomic layers. The core region consists of 13 atoms, including two nonequivalent atoms, both with a coordination number of 12.0. This core forms the first two layers, with a central atom surrounded by 12 equivalent and equidistant atoms, constituting the Au_{13} substructure. The remaining 42 atoms are located in the third shell, which is composed of interconnected (111) surface planes, each formed by six atoms. This outermost layer consists of surface atoms that are directly exposed to the vacuum. Within this layer, 12 atoms are positioned at the corners (vertex) with a coordination number of ~ 6.0, while the remaining 30 atoms are located along the edges and at the centers of the faces, each with a coordination number of ~ 8.0.

Figure S2a illustrates the models representing different chemical coordination environments, encompassing both finite and extended characteristics. For system (*i*), a close-packed Au (111) slab model was constructed using optimized bulk lattice constants. This model features a 3 × 3 surface unit cell in the periodic directions defined by the *xy*-plane and includes 4 layers stacked in the *z*-direction, with

sufficient separation between periodic images, ranging from approximately 17 to 20 Å of vacuum. For systems (*ii*) and (*iii*), a supercell approach was adopted, utilizing cubic boxes with dimensions of 25 Å and 20 Å, respectively. This configuration ensures a minimum distance of 15 Å between the systems and their periodic images. By incorporating both periodic and non-periodic system models, this approach provides a comprehensive representation of the chemical environments typically encountered by salt molecules on AuNPs.

For the atomic configurations involved in the molecular adsorption study, each supercell contained one saline molecule (mol=NaCl, $NaNO_3$, or Na_2SO_3) adsorbed onto substrate models (sub=Au (111), Au_{55}, or Au_{13}), forming the mol/subsystems. To explore the potential energy surface (PES) of the analyte-substrate interaction, the configurational space of molecular adsorption was examined to identify the most stable configurations and optimal orientational conformations. This was achieved through a strategy based on Ab-Initio Molecular Dynamics (AIMD) simulations.

The AIMD simulations commenced with atomic configurations where the molecules were arbitrarily oriented relative to the substrate. A thermalization process was then conducted at 300 K, followed by a simulated annealing process (ranging from 300 to 0 K). This annealing process provided sufficient thermal energy for the molecules to explore potential adsorption sites and subsequently freeze in the most stable configurations. In addition to the final AIMD configuration, snapshots were collected during the thermalization and simulated annealing phases, which were then structurally optimized using high-level quantum-mechanical calculations. Finally, the configurations resulting from the most stable adsorption were subjected to a stability check by achieving thermal equilibrium through additional AIMD simulations (as illustrated in **Figure S2b**).

Table S2 presents key results for individual and isolated systems, with the energy stability assessed using the formation energy concept:

$$E_f^{mol} = \frac{(E_{tot}^{mol} - mE_{tot}^{free-atoms})}{m} \tag{2}$$

and

$$E_f^{sub} = \frac{(E_{tot}^{sub} - nE_{tot}^{free-atoms})}{n} \tag{3}$$

where E_{tot}^{mol}, E_{tot}^{sub}, and $E_{tot}^{free-atoms}$ represent the total energies per atom for the molecules, substrates, and constituent free atoms, respectively. Here, m and n denote the number of atoms in the molecules and substrates, respectively. Negative values of formation energy indicate the energetic stability of the molecule or substrate formation. Additionally, the table includes structural properties such as equilibrium bond distances (d_0) for molecules and average bond lengths (d_{av}) along with the effective coordination number (ECN) for substrates. Vibrational frequencies (v) are provided for the molecules, while the total magnetic moment (m_T) is reported for the substrates.

We observed that, in addition to their inherent stability, the magnitudes of E_f for the substrate models increase proportionally with the coordination of the systems, following the order: Au(111)>Au_{55}>Au_{13}, as anticipated. Consequently, there is a statistically higher likelihood of forming Au(111)-type chemical environments, followed by Au_{55} and, lastly, Au_{13}, in experimentally synthesized AuNPs. Furthermore, lower coordination is reflected in more reactive environments, as evidenced by the higher m_T values. The substrate properties are consistent with those reported in the literature [90–95]. For the molecular systems, we observed excellent agreement with previously published data [96], with the largest discrepancies for E_f, d_0, and v being less than 3.7%, 1.2%, and 1.6%, respectively.

The investigation of the molecular adsorption process enables an understanding of the key aspects associated with the interaction in mol/subsystems, i.e., between salt molecules and Au-based substrates, for the lowest energy configurations (**Figure S2c**). Among the main properties analysed, our focus is on the adsorption energy (E_{ad}), which quantifies the binding energy of the combined system relative to the energies of the individual, separate systems. Alternatively, this energy can be decomposed into the interaction energy (E_{int}) between the molecules and substrates, which serves as an additive term, and the distortion energies of the molecules (E_{dist}^{mol}) and substrates (E_{dist}^{sub}), which act as non-additive terms. The adsorption energy is defined as:

$$\begin{aligned} E_{ad} &= E_{tot}^{mol/sub} - E_{tot}^{mol\ relaxed} \\ -E_{tot}^{sub\ relaxed} &= E_{int} + E_{dist}^{BAI} + E_{dist}^{sub} \end{aligned} \tag{4}$$

where $E_{tot}^{mol/sub}$, $E_{tot}^{mol\ relaxed}$, and $E_{tot}^{sub\ relaxed}$ represent the total energies of the mol/sub system, the gas-phase relaxed molecule, and the relaxed substrate, respectively. The remaining terms are defined as follows:

$$E_{int} = E_{tot}^{mol/sub} - E_{tot}^{mol\ frozen} - E_{tot}^{sub\ frozen} \tag{5}$$

which corresponds to the mol/sub binding energy without accounting for structural distortions upon adsorption/interaction process;

$$E_{dist}^{mol} = E_{tot}^{mol\ frozen} - E_{tot}^{mol\ relaxed} \tag{6}$$

And

$$E_{dist}^{sub} = E_{tot}^{sub\ frozen} - E_{tot}^{sub\ relaxed} \tag{7}$$

which represent the distortion energies calculated as the difference between frozen and relaxed structures. Here, the terms $E_{tot}^{mol\ frozen}$ and $E_{tot}^{sub\ frozen}$ are the total energies obtained from the frozen structures of the mol/sub systems in equilibrium. Finally, the formation energy of the adsorbed systems can be estimated as follows:

$$E_f = \frac{(mE_f^{mol} + nE_f^{sub} + E_{ad})}{(m+n)} \tag{8}$$

In addition to assessing the distortion energies, resulting from the mol-sub interaction, we also quantified the structural changes induced by this interaction by measuring the variations in average bond lengths of the molecules and substrates after adsorption/interaction (ads) compared to their respective values before adsorption. The percentage change in average bond length ($\Delta\, d_{av}$) is calculated as:

$$\Delta\, d_{av} = \frac{(d_{av,ads} - d_{av})\,.100}{d_{av}} \tag{9}$$

where $d_{av,ads}$ represents the average bond length after adsorption, and d_{av} is the average bond length before adsorption.

We also performed Bader's effective charge analysis to quantify the charge redistribution occurring during the interaction between the molecules (q^{mol}) and the substrate (q^{sub}). The results of this analysis are depicted in Fig. 6, with the corresponding numerical values provided in **Table S2**.

We observed from Fig. 6 (and **Table S2**) that the stabilization pattern of the mol/sub compound systems mirrors the trend observed for the individual substrates as indicated by E_f. Specifically, the stabilization of the combined systems increases with higher coordination of the substrates. This is evidenced by the stability trend: mol/Au (111)>mol/Au_{55}>mol/Au_{13}. This trend aligns with the stability of the individual substrates reported in Table 2.

In terms of molecular species, the stabilization pattern observed for the mol-sub combinations follows the trend:

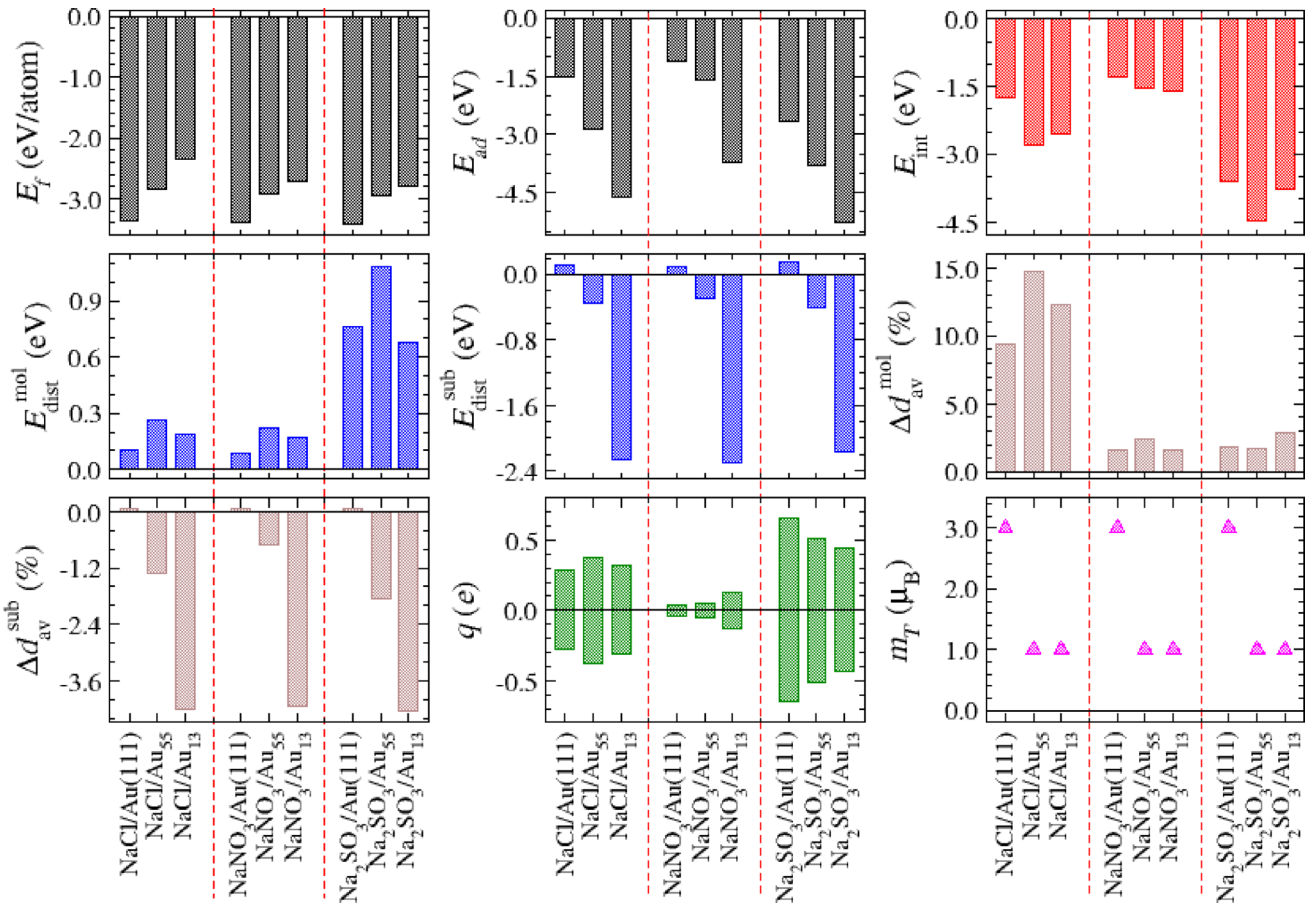

Fig. 6 Key mol/sub properties: formation energy (E_f), adsorption energy (E_{ad}), interaction energy (E_{int}), mol and sub distortion energies (E_{dist}^{mol} and E_{dist}^{sub}), mol and sub relative deviations in average bond lengths ($\Delta\, d_{av}^{mol}$ and $\Delta\, d_{av}^{sub}$), mol and sub effective Bader charge (q^{mol} and q^{sub}), and total magnetic moment (m_T)

Table 2 Individual system properties: formation energy (E_f), equilibrium bond distances (d_0), and vibrational frequencies (v) for mol=NaCl, $NaNO_3$, and Na_2SO_3; and E_f, average bond lengths (d_{av}), effective coordination number (ECN), and total magnetic moment (m_T) for sub=Au(111), Au_{55}, or Au_{13}

mol	E_f (eV/atom)	d_0 (Å)	v (cm^{-1})	
NaCl	−2.100	2.387 (Na-Cl)	355.2	
$NaNO_3$	−3.718	2.224 (2xNa-O), 3.832 (Na-O), 2.605 (Na-N), 1.272 (3xN-O)	1499.2, 1220.0, 991.1, 800.9, 727.0, 687.3, 317.8, 260.8, 118.1	
Na_2SO_3	−3.555	2.213 (2xNa-O), 2.170 (2xNa-O), 2.777 (Na-S), 1.567 (3xS-O)	973.3, 912.1, 715.8, 561.4, 547.3, 477.9, 340.5, 310.8, 293.4, 236.1, 95.8, 77.2	
sub	E_f (eV/atom)	d_{av} (Å)	ECN	m_T
Au (111)	−3.379	2.910	10.485	1.0
Au_{55}	−3.179	2.875	8.402	3.0
Au_{13}	−2.412	2.876	6.396	5.0

Na_2SO_3/sub>$NaNO_3$/sub>NaCl/sub. This indicates that the Na_2SO_3-sub interaction results in the highest stability, surpassing the interactions with $NaNO_3$ (which is the most stable molecule in the gas phase, as shown in Table 2).

The increased stability of AuNPs, when stabilized with Na_2SO_3, is primarily due to the formation of coordinate bonds between gold and sulfur atoms, which enhances electrostatic stability. This results in a stronger and more stable interaction compared to those with $NaNO_3$ or NaCl. The Au-S coordinate bonding contributes significantly to the stabilization of the NPs through electrostatic interactions. The presence of sulfur atoms introduces a favourable charge distribution that interacts effectively with the gold surface, thereby enhancing the overall stability of the AuNPs.

In colloidal systems, the zeta potential is often used as an indicator of NPs stability. A more negative zeta potential typically signifies better stability, as it reflects stronger electrostatic repulsion between particles, which helps prevent aggregation. Among the AuNPs stabilized with saline molecules, all systems exhibited at least moderate stability in terms of zeta potential. However, the most favourable result was obtained with Na_2SO_3, which had a zeta potential of −51.23 mV, while the minimum values were observed for $NaNO_3$.

This enhanced stability with Na_2SO_3 can be attributed to the strong coordinate bonding between gold and sulfite anions due to its higher surface charge density, which contributes to the system's overall electrostatic stability. The strong Au-S interactions and the resulting charge distribution provide a more stable colloidal system compared to those stabilized with $NaNO_3$.

In the context of AuNPs and the adsorption of different salts (NaCl, $NaNO_3$, Na_2SO_3), both the maximum absorbance and stability can be influenced by the nature of the adsorbed species and their interaction with the NPs. In contrast to E_f, the E_{ad} reveals an inverse trend for the three salt molecules with respect to the substrates. Specifically, the E_{ad} magnitude is more pronounced on less coordinated substrates, reflecting the increased reactivity of low coordination sites. Thus, we have a E_{ad} magnitude that follows: mol/Au_{13}>mol/Au_{55}>mol/Au (111). Consequently, regions of AuNPs with corner (vertex) topologies exhibit more intense interactions, followed by regions of edges, with the least interaction occurring on planar (face) regions.

The stability of adsorbed molecules on gold nanoparticles is influenced by the strength and nature of their interactions with the NPs surface. Among the salts studied, Na_2SO_3 demonstrates a more favourable interaction with AuNPs compared to NaCl or $NaNO_3$, leading to more stable adsorption. This observation is reflected in the E_{ad}, where the modulus follows the trend: Na_2SO_3/sub>NaCl/sub>$NaNO_3$/sub. This trend is consistent with experimental results for maximum absorbance, confirming that sulfur-based mol/subsystems exhibit superior stabilization due to more intense molecular adsorption.

Consequently, our findings support that the interaction between AuNPs and Na_2SO_3 involves the formation of coordinate bonds between Au and the SO_3^{2-}. This interaction significantly alters the NPs surface and charge distribution, leading to enhanced stability. The more negative zeta potential observed with Na_2SO_3 suggests improved electrostatic repulsion, which helps prevent aggregation and contributes to the overall stability of AuNPs in the colloidal system.

The nitrogen-based mol/subsystems, which 1rank second in stability, might intuitively be expected to exhibit a corresponding magnitude of adsorption. Contrary to this expectation, the chlorine-based molecular systems occupy this position. This discrepancy arises because systems with nitrogen demonstrate a more neutral interaction compared to the three salt molecules studied. This observation is attributed to the higher formation energy of nitrogen-based molecules (as shown in Table 2), which contributes to the overall formation energy of the adsorbed system, combined with lower charge exchange. This interplay will be further analysed in subsequent discussions.

To further explore the stabilization dynamics during molecular adsorption, we conducted an energetic decomposition analysis. This analysis revealed that a higher magnitude of E_{ad} is directly associated with a greater magnitude of E_{int}. This relationship, coupled with the energetic penalties and stabilizations due to molecular interaction and estimated distortion energies, elucidates the adsorption energy

results for systems representing various chemical environments of AuNPs.

Our findings indicate that molecular interaction with the substrates consistently incurs penalties due to structural distortions in the molecules, with sulfur-based systems showing the most pronounced effects. For the high-coordination substrate, Au(111), the distortion in the substrates appears to be non-additive. In contrast, for the low-coordination substrates (Au_{55} and Au_{13}), structural distortions in the substrates result in energetic gain, which intensify as the substrate coordination decreases. This suggests that a structural reconstruction of the Au atomic cluster occurs, optimizing it to enhance molecular interactions.

The local impact of structural distortions in both molecules and substrates, as revealed by the corresponding distortion energies, is further evidenced by the relative deviations in the average bond lengths ($\Delta\, d_{av}^{mol}$ and $\Delta\, d_{av}^{sub}$). We observed an expansion of the equilibrium bond lengths for all molecules following adsorption, with the NaCl molecule exhibiting a particularly pronounced expansion. For the substrates, the Au(111) surface shows an almost negligible expansion after adsorption. In contrast, the substrates characterized by Au_{55} and Au_{13} undergo distortions that lead to a contraction in the average bond lengths compared to those in isolated nanoclusters. This observation confirms that, unlike the planar regions (Au(111)), there is a surface reconstruction in the low-coordination regions of AuNPs (Au_{13} and Au_{55}).

In all the analysed systems, charge transfer during the molecular adsorption process consistently occurs from the molecule to the substrate. Bader analysis confirms this, indicating the presence of cationic molecules and anionic substrates, as expected. Notably, sulfur-based systems exhibit the most significant charge exchanges, whereas nitrogen-based systems show comparatively smaller exchanges. Figure 7 illustrates this through isosurfaces of charge differences, highlighting regions of charge concentration and depletion.

Our theoretical findings further underscore the significant influence of sodium counter-ions in the formation and stabilization of AuNPs. The SO_3^{2-} and Cl^- ions exhibit strong electrostatic interactions, playing a crucial role during both the vapor phase and NPs formation. In contrast, NO_3^- ions appear to exert a neutral or even slightly negative impact on the process.

The dominant stabilizing interaction observed is the formation of Au-S bonds, which is critical in establishing the electrostatic configuration of the molecule on the NPs surface. This configuration is particularly effective in preventing aggregation, as it generates repulsive forces between neighbouring, similarly protected NPs. On the other hand, systems involving nitrogen-based molecules display a more neutral interaction, characterized by minimal charge exchange between the molecule and substrate, highlighting their less significant role in nanoparticle stabilization.

The magnetic moment values of the AuNPs undergo notable changes as a result of molecular adsorption. For low-coordination systems such as Au_{13} and Au_{55}, which initially exhibit high total magnetic moments (5.0 μ_B and 3.0 μ_B, respectively), the adsorption of molecules leads to

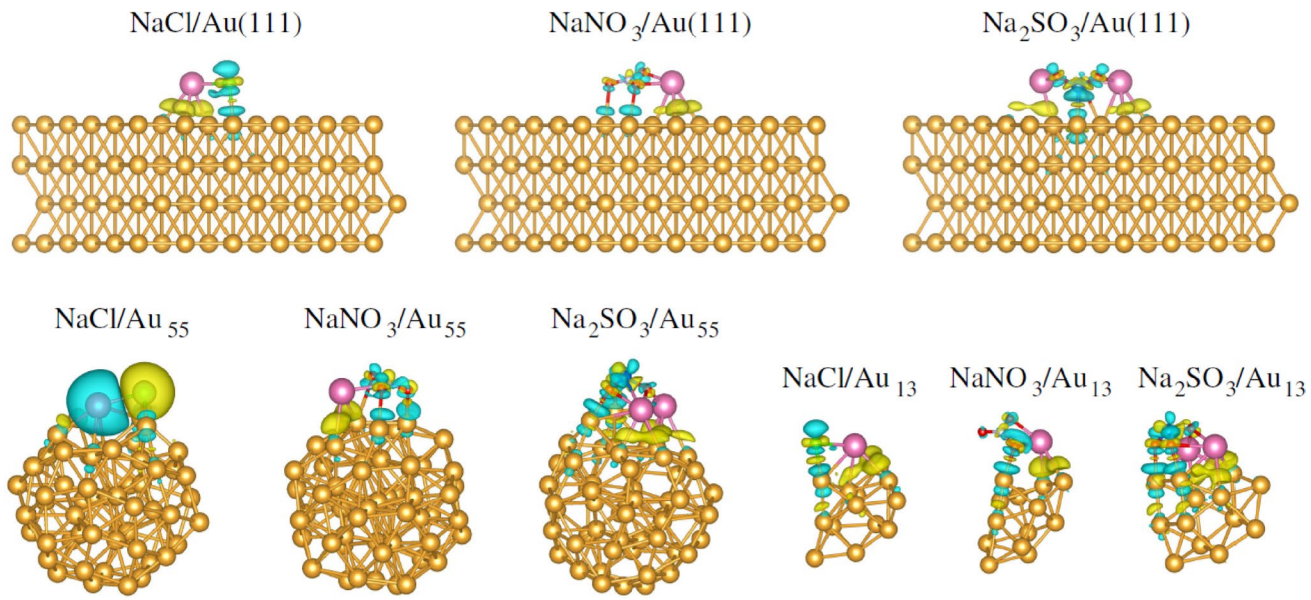

Fig. 7 Charge density difference plots for the lowest energy conformations: NaCl/Au(111), $NaNO_3$/Au(111), Na_2SO_3/Au(111), NaCl/Au_{55}, $NaNO_3$/Au_{55}, Na_2SO_3/Au_{55}, NaCl/Au_{13}, $NaNO_3$/Au_{13}, and Na_2SO_3/Au_{13}. The isosurface value is set to 0.003 for all cases. The Na, Cl, N, S, O, and Au atoms are represented by dark pink, green, grey, blue, red, and light-washed orange colours, respectively. Cyan and yellow isosurfaces denote charge depletion and accumulation regions, respectively

a significant reduction in these values, dropping to approximately 1.0 μ_B. This considerable decrease is attributed to the formation of molecular bonds and the extensive geometric restructuring of the nanoclusters induced by the adsorption process.

In contrast, pristine Au surfaces, which initially possess a low total magnetic moment (1.0 μ_B), experience an increase in magnetic moment values upon molecular adsorption, rising to about 3.0 μ_B. This increase underscores the crucial role that the adsorbed molecules play in activating the adsorption sites, thereby enhancing the reactivity of the gold surface. The interplay between molecular adsorption and magnetic moment alterations highlights the dynamic nature of these systems, where molecular interactions can either quench or enhance the magnetic properties depending on the coordination and structural configuration of the gold substrates.

4.1 Colloidal Stability

Thus, to understand and compare the long-term behaviour of the systems, UV-Vis spectroscopy analyses were conducted, along with PPI calculations, following the method outlined by Merk et al. (2014) [34]. The systems were evaluated over three months, with analyses performed every 15 days without sonication, under three different storage conditions: in a translucent vial exposed to ambient light (10 W, 6,500 K, daylight spectrum with minimal UV emission), in an amber vial also exposed to ambient light, and in a translucent vial stored in a refrigerator. The UV-Vis spectra corresponding to these analyses are provided in the supplementary information (**Figure S3**, **S4**, and **S5**).

The tendency of aggregation, as measured by PPI, and the variation in the LSPR peak over time are illustrated in Fig. 8. The combination of salts significantly influences the aggregation behaviour, with systems containing Cl and S exhibiting greater instability compared to those with a combination of these with N. In this context, N system shows a neutral behaviour, similar to the system in ultrapure water (W), as depicted in Fig. 8a and d. Conversely, the presence of salts like ClN and ClNS appears to counterbalance charges, resulting in more stable systems compared to those with only Cl or S. Although certain systems display relatively high standard deviation values, a discernible trend in the variation of absorbance in the LSPR can still be observed. This parameter is especially valuable for evaluating colloidal stability, as it offers a direct, sensitive, and non-invasive method for detecting changes in interparticle distance, surface charge, and environmental conditions. Consequently, given the observed loss of stability after 60 days, the variation in LSPR serves as a reliable indicator of aggregation. The resulting stability trend is as follows: ClN S = ClN > W = N = NS > S > ClS > Cl.

Merk et al. [34] identified thiocyanate (SCN^-) as a strongly chaotropic anion, exhibiting exceptional stabilization of ligand-free AuNPs at ultralow ionic strengths (<20 µM), with a steep rise in the PPI attributed to its high polarizability and weak hydration. Their work highlighted

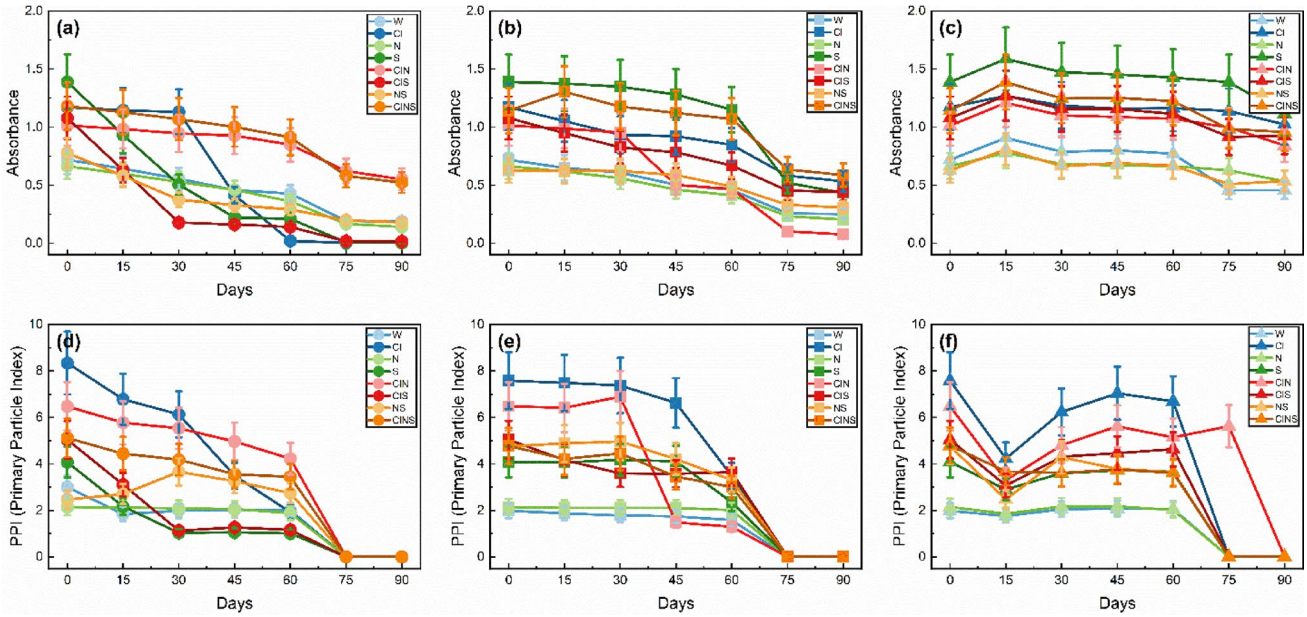

Fig. 8 Study of colloidal stability through LSPR monitoring and PPI calculation: (**a**) LSPR variation in a translucent vial exposed to ambient light, (**b**) LSPR variation in an amber vial exposed to ambient light, (**c**) LSPR variation in a translucent vial stored in a refrigerator, (**d**) PPI variation in a translucent vial exposed to ambient light, (**e**) PPI variation in an amber vial exposed to ambient light, and (**f**) PPI variation in a translucent vial stored in a refrigerator. Data represent the mean of three independent experiments ($n = 3$). Error bars indicate the standard deviation (SD)

SCN^-'s adsorption-driven stabilization, surpassing chloride and nitrate, and linked this to its unique ion-specific behavior. In contrast, our study investigates sulfite (SO_3^{2-}), a sulfur-containing anion with distinct chemical behavior. While SCN^- relies on its chaotropic nature and polarizability to enhance electrostatic repulsion, sulfite demonstrates a dual stabilization mechanism: (1) strong Au-S coordination via π-back bonding, as supported by DFT simulations, and (2) suppression of surface oxidation (evidenced by XPS), which reduces aggregation-prone oxidized Au species. Unlike SCN^-, which destabilizes at higher ionic strengths due to charge screening, sulfite maintains colloidal stability even in mixed-salt systems (e.g., ClS, ClNS), suggesting synergistic interactions. Both anions underscore the critical role of sulfur in ligand-free stabilization, yet sulfite's ability to chemically passivate the AuNP surface offers a unique advantage for applications requiring long-term oxidative resistance. This expands Merk's framework by illustrating how anion-specific chemical interactions, beyond polarizability and hydration, govern colloidal stability in sulfur-rich systems.

AuNPs synthesized in ultrapure water often exhibit reduced colloidal stability due to the absence of stabilizing ionic interactions. In such environments, stabilization relies solely on the surface charge of the nanoparticles, resulting in weak electrostatic repulsion that is insufficient to counteract intermolecular attractive forces. The introduction of salts enhances colloidal stability by introducing ionic species that interact with the nanoparticle surfaces, modifying the electric double layer and introducing hydration forces [32]. For example, kosmotropic ions (e.g., S^{2-}) are known to strengthen hydration shells and promote stability, whereas chaotropic ions (e.g., Cl^-) can disrupt water structuring and induce aggregation. Mixed-salt systems, such as those incorporating Cl^- and S^{2-} ions, leverage the balance between these opposing effects to optimize stabilization. Additionally, specific ion adsorption mechanisms, which depend on ion size, charge, and hydration properties, significantly influence nanoparticle stability at low salinities [34].

Figure 8b and e show the behaviour of the systems stored in an amber vial, which reduces light interaction while maintaining the same temperature as the translucent environment. A trend of decreasing stability over time is observed, although it is less pronounced compared to the system in the translucent vial. Notably, significant destabilization occurs after 60 days, with the ClN system becoming more unstable than the ClS system, reversing the behaviour seen under light exposure. This suggests that the LSPR phenomenon alone cannot fully account for the observed agglomeration. However, the effects of LSPR on the ClN and ClS systems remain relevant, as the ClN system appears more sensitive to light compared to the ClS system, and vice versa.

The interplay of different salts significantly influences the aggregation behaviour of the system, either promoting or reducing it. Systems containing N generally exhibit lower stability, with isolated N showing neutral behaviour similar to the system without salts (W). This observation aligns well with computational simulations. However, when N is combined with other salts, it acts as a charge counterbalance, enhancing stability. This effect is particularly evident in systems such as ClS and NS, as well as in the presence of all salts combined (ClNS). Despite these observations, most systems demonstrate relatively high standard deviation values, complicating the identification of clear trends in the variation of absorbance associated with localized surface plasmon resonance (LSPR). Nonetheless, within the context of these deviations, a subtle distinction between the two groups can be discerned. When evaluating long-term stability over 60 days using LSPR for the amber vial condition, the stability trend is as follows: S = ClNS = Cl = ClS > NS = ClN = W = N.

Notably, the behaviour of systems stored in amber vials, which reduce light exposure, reveals a slower decrease in stability over time compared to those in translucent environments. The ClN system, despite being more sensitive to light exposure, became less stable than the ClS system after 60 days in darkness, suggesting that light is a contributing but non-dominant factor in the aggregation process. This further implies that other mechanisms, such as electrostatic and hydration forces, play significant roles in governing colloidal stability. The destabilization trends, confirm that the combination of salts directly influences long-term colloidal behaviour, particularly for systems such as ClNS, which maintain higher stability.

The observed loss of stability under illumination arises primarily from exposure to ambient fluorescent light. The evolution of PPI values over 60 days indicates a mean degradation rate of approximately 0.8 PPI units $month^{-1}$ (≈45% total reduction), confirming that visible light accelerates aggregation compared with amber (~20%) or refrigerated (~10%) conditions. Since PPI quantitatively reflects the ratio of dispersed to aggregated nanoparticles, this decline accurately represents the light-induced destabilization of the colloid. The degradation rate was derived from the slope of the PPI–time curves in Fig. 8d–f, which depict the variation in absorbance ratio (A_{380}/A_{800}) as a function of storage time. Under light exposure, PPI decreased from initial values around 4.2 ± 0.3 to 2.3 ± 0.4 after 60 days, while amber and refrigerated conditions retained higher PPI values of ≈3.4 ± 0.2 and 3.8 ± 0.1, respectively. These quantitative changes correspond to relative degradation rates of roughly 0.032, 0.013, and 0.006 PPI day^{-1} for the three conditions, establishing a clear hierarchy of stability loss (Light > Amber > Refrigerated).

Table 3 Analysis of variance for the applied models describing long-term stability

Source	Degree of Freedom	Adjusted Sum of Square	Adjusted Mean Square	F Value	*p*-Value
Fitted with quadratic model					
PPI Under Light					
Model	5	8.8827	1.1103	7.6331	0.0625
Lack-of-fit	1	0.0242	0.0242		
Pure Error	2	0.6232	0.3116		
Fitted with quadratic model					
PPI Amber flask					
Model	5	4.6400	0.5800	52.5191	0.0040
Lack-of-fit	1	0.0125	0.0125		
Pure Error	2	0.0400	0.0200		
Fitted with a linear model					
PPI Refrigerator					
Model	2	13.1380	1.6422	19.7682	0.0023
Lack-of-fit	4	1.6087	0.4022		
Pure Error	2	0.1224	0.0612		

This trend aligns with the statistical mixture-design models presented in Table 3, where the PPI data under light required a quadratic fit ($p=0.0625$), indicating non-linear degradation behavior typical of aggregation-dominated kinetics. In contrast, the amber and refrigerated conditions followed statistically significant models ($p=0.0040$ and $p=0.0023$, respectively), showing slower, near-linear degradation rates consistent with diffusion-controlled particle coalescence rather than photochemically driven destabilization. Together, the experimental data and statistical analysis demonstrate that light exposure accelerates aggregation primarily through visible-light-induced surface charge rearrangement, while lower temperature and reduced illumination slow the kinetic pathway of nanoparticle growth and sedimentation.

Figure 8c illustrates a clear stability trend over time, with the colloidal systems remaining stable and only exhibiting destabilization after approximately two months. This indicates that even when stored under controlled conditions, such as being shielded from light and maintained at low temperatures, PPI values can fluctuate, with 60 days representing the limit of colloidal stability. Beyond this period, AuNPs tend to aggregate, likely due to particle aggregation or disruptions in electrostatic equilibrium. Notably, as shown in Fig. 8f, both LSPR and PPI values increased shortly after synthesis. This increase is attributed to ripening effects, where non-plasmonic nanoclusters smaller than 2 nm, formed during ablation, undergo growth into larger

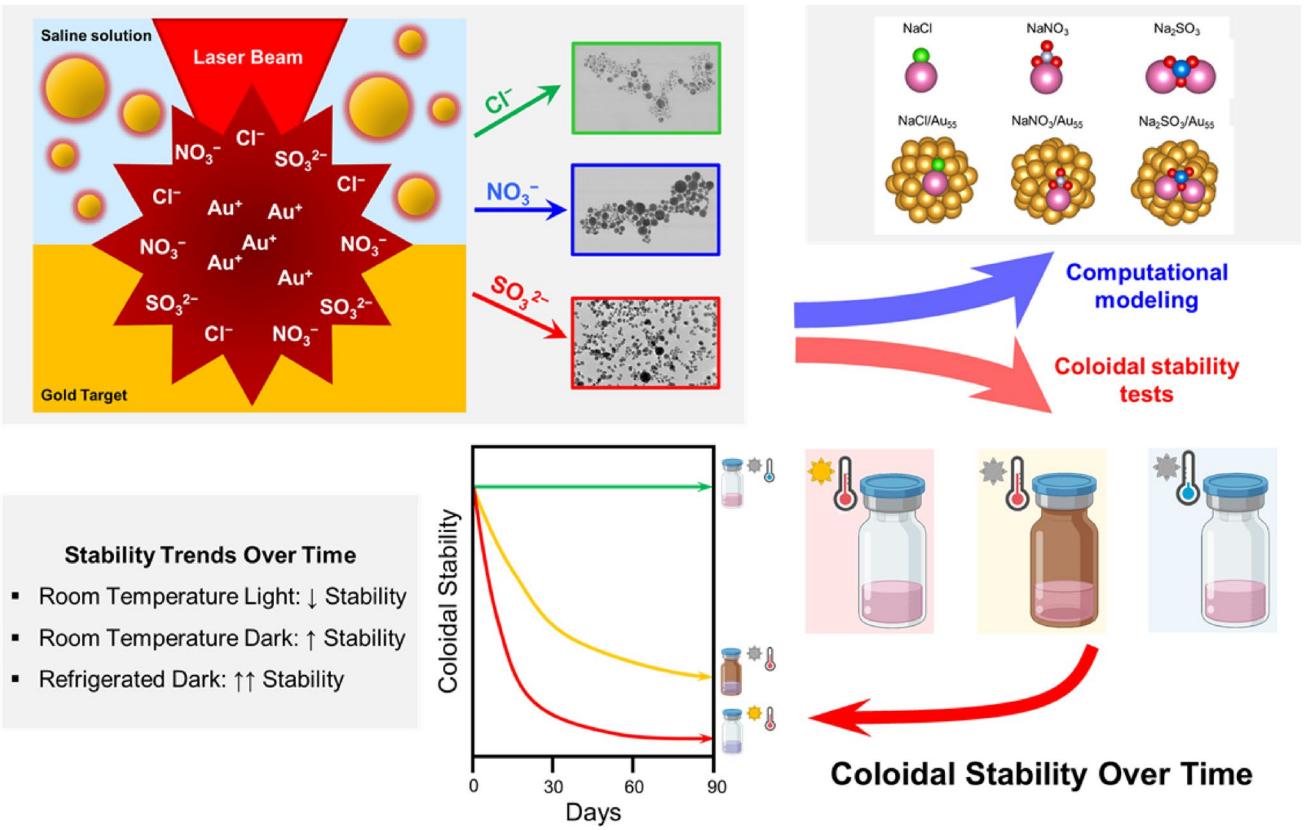

plasmonic nanoparticles via coalescence and Ostwald ripening. This process enhances the colloid's plasmonic properties, consistent with previously observed growth mechanisms in analogous systems [97].

Previous studies [30, 34, 84] have reported the colloidal stabilization of AuNPs solutions using NaCl and other salts. In this study, we present long-term results over three months. We observed that the AuNPs begin to settle after two months, even when PPI values are high, indicating that PPI does not significantly influence aggregation trends after 60 days. Thus, based on the LSPR evaluation after two months, the stability order is as follows: S > ClNS = Cl = ClS = ClN > W = N = NS, aligning well with computational modelling results.

Our analyses simulate shelf storage trends under different conditions, revealing that while light does influence the PPI values of the systems, it is not the sole factor to consider when assessing long-term colloidal stability. The combination of darkness and low temperatures, as under refrigeration condition, appears to have a more significant impact on reducing aggregation. Furthermore, as indicated by computational simulations, optimal results were achieved in systems stored without light exposure. This underscores that adsorption and electrostatic interactions are the primary mechanisms governing the colloidal stability of NPs.

While the PPI parameter provided a robust and quantitative means to monitor aggregation and relative dispersion over time, its reliability as a single proxy for colloidal stability becomes limited beyond approximately 60 days. This limitation stems from the fact that PPI is derived exclusively from optical absorption ratios and therefore does not account for phenomena such as sedimentation or the formation of non-plasmonic aggregates that fall outside the optical detection path. Consequently, systems may still exhibit high PPI values even as visible settling and partial agglomeration occur, as noted in Fig. 8d–f. To complement this observation, a new figure has been added to the Supporting Information (**Figure S6**), presenting photographs of the eight colloidal systems taken 15 days after synthesis. These images reveal early aggregation and partial agglomeration, reinforcing that PPI should be interpreted alongside visual or turbidity-based indicators to more comprehensively assess long-term colloidal stability.

The apparently stronger stabilization observed for AuNPs synthesized in mixed-anion media (SO_3^{2-} + Cl^- or SO_3^{2-} + NO_3^-) arises from a synergistic interfacial effect rather than from additive stabilization. Although DFT calculations show that SO_3^{2-} binds more strongly to Au surfaces than either Cl^- or NO_3^- individually, the coexistence of these anions induces charge redistribution and electrostatic coupling at the Au/solution interface. Specifically, SO_3^{2-} system donates electron density to under-coordinated Au sites, while Cl^- or NO_3^- systems modulate the local electrostatic potential and occupy neighboring weakly bound regions, producing a more homogeneous, negatively charged interfacial layer. This cooperative arrangement enhances the electrostatic repulsion between nanoparticles and suppresses aggregation, resulting in smaller particle sizes. Thus, the experimental trend reflects a genuine synergistic stabilization mechanism, combining strong chemisorption (SO_3^{2-}) with diffuse electrostatic screening by monovalent anions.

5 Statistical Analyses

5.1 *Long-Term* Stability

Statistical tools are particularly valuable for analysing the effects of mixtures on colloidal stability. The PPI is a critical parameter for assessing the stability of colloidal systems, as it provides quantitative insight into particle aggregation and dispersion behaviour. **Table S3** summarizes the PPI responses recorded after 60 days, categorized by the type of system produced and the storage environment. The systems were further monitored over 90 days under three distinct storage conditions. It is important to note that the samples were not shaken or sonicated before UV-Vis analysis, simulating the effects of shelf storage. The potential effects of redispersion using ultrasonic baths or similar methods were not evaluated. The analysis of variance for significant systems ($p < 0.05$) is provided in Table 3, along with linear regression coefficients and correlation coefficients detailed in **Table S4**.

Correlation models for stability were evaluated using the PPI at the 60-day threshold of colloidal stability, revealing distinct statistical trends influenced by storage conditions. For samples exposed to artificial light, no statistically significant correlation ($p < 0.05$) was observed, necessitating the application of a quadratic model for the optimal representation of data. Conversely, samples stored in amber vials exhibited a statistically significant quadratic trend, while those maintained under refrigerated conditions demonstrated a statistically significant linear pattern. These observations underscore the complex interplay between environmental factors and the stability of colloidal systems.

Figure S7a illustrates the stability outcomes for AuNP systems exposed to artificial light. In this scenario, mixtures containing NaCl and $NaNO_3$ maintained PPI values above 4, indicative of enhanced stability. In contrast, systems enriched with Na_2SO_3 exhibited increased sensitivity to light, suggesting a heightened susceptibility to destabilizing influences. Although the model for this condition did not achieve statistical significance, the observed trend indicating that mixtures of NaCl and $NaNO_3$ positively influence

PPI values provides valuable insights into the stabilizing effects of these salts under illuminated conditions.

Figure S7b displays the stability results for systems stored in amber vials under artificial light. Under these conditions, the behaviour of NaCl and $NaNO_3$ mixtures diverges from that observed in translucent vials, with a negative impact on PPI values compared to mixtures containing Na_2SO_3. This observation highlights the importance of container opacity and its role in modulating the interaction between light and the colloidal system.

Figure S7c presents the stability outcomes for samples stored under refrigerated conditions. Notably, the behaviour of these systems mirrors that observed on the synthesis day, with refrigerated storage effectively preserving the initial colloidal stability. This suggests that refrigeration, particularly when samples are shielded from light, may represent the optimal condition for maintaining the long-term stability of AuNP systems.

The synthesis of the salt-free system based on ultrapure water (W) demonstrated moderate stability across all evaluated storage conditions but did not exceed the performance of other systems, as observed in **Table S3**. Under light exposure, W exhibited greater stability compared to systems containing sulfur (S) or nitrogen (N) individually, although it was less stable than systems incorporating chlorine (Cl), chlorine-nitrogen (ClN), or certain multicomponent formulations. When stored in amber flasks, W displayed reduced stability relative to most other systems, including those containing Cl, S, or multicomponent combinations, indicating diminished effectiveness in environments with limited light exposure. Under refrigeration, W maintained consistent stability; however, it was outperformed by all other systems, particularly those containing Cl, ClN, or advanced multicomponent formulations, which demonstrated superior stability under these conditions.

The observed variations in the PPI of AuNPs under different storage conditions can be attributed to the combined influence of environmental factors, including light exposure, temperature, and the nature of the stabilizing salts. The PPI serves as an indicator of colloidal system stability, with higher values signifying enhanced stabilization. The results indicate that salts such as NaCl and $NaNO_3$ demonstrate stabilizing effects under light exposure, likely due to their ability to strengthen the electrostatic double-layer repulsion around the nanoparticles. In contrast, systems containing Na_2SO_3 exhibited increased sensitivity to light, potentially owing to the weaker stability of the electrostatic layers formed by sulfite ions in illuminated environments.

The pronounced differences in PPI trends between samples stored in translucent and amber vials underscore the critical influence of light on the destabilization of colloidal systems. Amber vials, which limit light exposure, provided enhanced stability for certain salt combinations, such as Na_2SO_3-based systems. However, the contrasting behaviours of NaCl and $NaNO_3$ mixtures under translucent and amber conditions highlight the complex, salt-specific effects of light on stabilization mechanisms.

Refrigeration proved to be the most effective storage condition for maintaining colloidal stability, as evidenced by linear PPI trends and sustained stability over 60 days. Lower temperatures reduce the kinetic energy of nanoparticles, thereby minimizing collision frequency and aggregation risk. The consistent PPI values observed in refrigerated systems, regardless of the salt composition, suggest that refrigeration mitigates destabilizing factors such as light exposure and electrostatic imbalances. These findings highlight the importance of optimizing storage conditions through a combination of refrigeration and light shielding, as well as the careful selection of stabilizing salts, to achieve long-term colloidal stability of AuNP systems.

6 Conclusions

In this study, we employed PLAL to directly produce ligand-free, contamination-free AuNPs in simple saline media, embodying a truly green-chemistry approach. By avoiding chemical reductants and post-synthesis purification, PLAL generates ultrapure colloids whose physicochemical properties can be tuned simply by the choice of counter-ion.

The computational simulation analyses further revealed that the SO_3^{2-} counter-ion exerts a more substantial influence on the Au NPs compared to Cl^- and NO_3^- ions, due to sulfur complexation affinity to gold atoms, which helps to minimize oxidation of the Au NPs. In addition, XPS analysis demonstrated that Au NPs in system N exhibited a 60% increase in oxidized sites compared to those in system W. Conversely, AuNPs produced in sulfur-containing saline mixtures showed an increase in the Au reduction state by up to 6.9%.

To translate these insights into practical guidelines, we carried out a rigorous three-month shelf-life study, monitoring PPI every 15 days under (i) ambient light, (ii) reduced light in amber vials, and (iii) refrigeration. Statistical mixture-design models showed no significant trend under ambient light, a quadratic dependence on salt composition in amber vials, and a clear linear decline under refrigeration, establishing a ~60-day stability threshold for optimal storage. Together, this integrated experimental–computational framework deepens our understanding of ion-mediated nanoparticle stabilization and furnishes quantitative storage protocols. These findings pave the way for scalable production and reliable distribution of high-quality AuNP colloids for biotechnological, electronic, and catalytic applications.

Supplementary Information The online version contains supplementary material available at https://doi.org/10.1007/s40684-025-00837-7.

Acknowledgements This study was supported by CNPq (grants 403090/2022-9 and 409269/2023-9). CNPq are also thanked for the scholarships and fellowships granted to the authors. This work was funded by the European Regional Development Fund through the Operational Competitiveness Program and the National Foundation for Science and Technology of Portugal (FCT) under the projects UID/CTM/00264/2020 of the Centre for Textile Science and Technology (2C2T) and its base (https://doi.org/10.54499/UIDB/00264/2020, accessed on 1 May 2024) and programmatic (https://doi.org/10.54499/UIDP/00264/2020) components. M. J. P. thanks FAPERGS (grant number 24/2551-0001551-5) and CNPq (grants number 307345/2021-1 and number 444431/2024-1). XPS investigations have been financed by the Romanian Ministry of Education and Research under Nucleus program PNCDI 2023–2027, contract n° 30 N/2023. Also, the authors thank to Nanogreen for sharing the gold target, and Linden/EQA-UFSC for technical support with XRD characterizations.

Author Contributions P.C.R.: Conceptualization, Methodology, Investigation, Data curation, Formal analysis, Writing – Original draft; C.R.V.: Methodology, Investigation, Data curation, Formal analysis, Writing – Original draft; M. J. P.: Conceptualization, Methodology, Investigation, Data curation, Formal analysis, Writing – Original draft; D. C. C.: Writing – review & editing; J. P.: Data curation, Formal analysis, Writing – review & editing; A. Z.: Writing – review & editing; V. S.: Methodology, Data curation, Writing – review & editing; G. D.: Writing – review & editing; O. C.: Writing – review & editing; C. L. J.: Writing – review & editing; F.S.S.: Supervision, Resources, Funding acquisition, Project administration, Writing – review & editing; M.C.F.: Conceptualization, Supervision, Validation, Resources, Funding acquisition, Project administration, Writing – review & editing.

Data Availability The authors confirm that the data supporting the findings of this study are included within the article and its Supporting Information. Furthermore, raw data that underpin the results of this study are available from the corresponding author upon reasonable request.

Declarations

Competing Interest The authors declare that there are no financial or personal relationships that could have influenced the research presented in this manuscript.

References

1. Yanalak, G., Doganay, F., Eroglu, Z., et al. (2021). Ternary nanocomposites of mesoporous graphitic carbon nitride/black phosphorus/gold nanoparticles (mpg-CN/BP-Au) for photocatalytic hydrogen evolution and electrochemical sensing of paracetamol. *Applied Surface Science, 557*, 149755. https://doi.org/10.1016/J.APSUSC.2021.149755
2. Syrek, K., Czopor, J., Topa-Skwarczyńska, M., et al. (2023). Photoelectrochemical properties of BODIPY-sensitized anodic TiO2 layers decorated with AuNPs for enhanced solar performance. *The Journal of Physical Chemistry C, 127*, 9471–9480. https://doi.org/10.1021/acs.jpcc.3c00931
3. Lemoine, P., Dooley, C., Morelli, A., et al. (2022). AFM study of organic ligand packing on gold for nanoparticle drug delivery applications. *Applied Surface Science*, *574*, 151386. https://doi.org/10.1016/J.APSUSC.2021.151386
4. Heris, N. N., Baghani, L., Khonsari, F., et al. (2023). Delivery of EGFR-siRNA to prostatic cancerous cells based on polydopamine coated gold nanoparticles. *Journal of Drug Delivery Science and Technology*, *87*, 104869. https://doi.org/10.1016/j.jddst.2023.104869
5. Mishra, A., Ferhan, A. R., Ho, C. M. B., et al. (2020). Fabrication of plasmon-active polymer-nanoparticle composites for biosensing applications. *International Journal of Precision Engineering and Manufacturing-Green Technology, 8*(3), 945–954. https://doi.org/10.1007/S40684-020-00257-9
6. Harisha, B. S., Akkinepally, B., Vijayalakshmi, L., & Lim, J. (2025). Nanomaterial-Enhanced Electrochemical Biosensing of Breast Cancer Biomarkers: A Review of Innovations in Materials, Mechanisms, and Clinical Potential. International Journal of Precision Engineering and Manufacturing-Green Technology 2025 1–30. https://doi.org/10.1007/S40684-025-00793-2
7. Ricardo, P. C., Vanoni, C. R., Lima, A. R. S., et al. (2025). Tailored ligand-free gold nanoparticles: Exploring green synthesis in saline media for the electrochemical sensing of serotonin. *Electrochimica Acta*, *532*, 146483. https://doi.org/10.1016/j.electacta.2025.146483
8. Ouyang, X., Jia, N., Luo, J., et al. (2023). DNA nanoribbon-assisted intracellular biosynthesis of fluorescent gold nanoclusters for cancer cell imaging. *JACS Au, 3*, 2566–2577. https://doi.org/10.1021/jacsau.3c00365
9. Fu, Y. F., & Zhu, J. (2025). Current and future opportunities for lateral flow immunoassay strips based on tunable plasmonic properties of gold nanoparticles. *Microchimica Acta, 192*(8), 1–23. https://doi.org/10.1007/S00604-025-07352-1
10. Duman, H., Akdaşçi, E., Eker, F. (2024). Gold Nanoparticles: Multifunctional Properties, Synthesis, and Future Prospects. Nanomaterials 2024, Vol 14, Page 1805 14:1805. https://doi.org/10.3390/NANO14221805
11. Grys, D. B., De Nijs, B., Salmon, A. R., et al. (2020). Citrate coordination and bridging of gold nanoparticles: The role of gold adatoms in AuNP aging. *ACS Nano, 14*, 8689–8696. https://doi.org/10.1021/acsnano.0c03050
12. Marcelino, M. Y., Borges, F. A., Scorzoni, L., et al. (2021). Synthesis and characterization of gold nanoparticles and their toxicity in alternative methods to the use of mammals. *Journal of Environmental Chemical Engineering*, *9*, 106779. https://doi.org/10.1016/j.jece.2021.106779
13. Lee, J. C., Kim, W., & Choi, S. (2017). Fabrication of a SERS-encoded microfluidic paper-based analytical chip for the point-of-assay of wastewater. *International Journal of Precision Engineering and Manufacturing-Green Technology,* (2), Article 4:221–226. https://doi.org/10.1007/S40684-017-0027-9
14. Costa, D.C., Fernandes, M., Moura, C. et al. Laser ablation in liquid-assisted synthesis of three types of nanoparticles for enhanced antibacterial applications. Int. J. of Precis. Eng. and Manuf.-Green Tech. 12, 1699–1717 (2025).https://doi.org/10.1007/s40684-025-00711-6
15. Shabalina, A. V., Svetlichnyi, V. A., & Kulinich, S. A. (2022). Green laser ablation-based synthesis of functional nanomaterials for generation, storage, and detection of hydrogen. *Current Opinion in Green and Sustainable Chemistry*, *33*, 100566. https://doi.org/10.1016/j.cogsc.2021.100566
16. Ricardo, P. C., Nicolodelli, G., Fredel, M. C., et al. (2025). Tunable photoluminescence of graphene quantum dots synthesized via laser ablation in ethanol. *Journal of Luminescence, 281*, 121186. https://doi.org/10.1016/J.JLUMIN.2025.121186
17. Piotto, V., Litti, L., & Meneghetti, M. (2020). Synthesis and shape manipulation of anisotropic gold nanoparticles by laser ablation

in solution. *Journal of Physical Chemistry C*, *124*, 4820–4826. https://doi.org/10.1021/acs.jpcc.9b10793
18. Hassan, N. K., Khalid, F. G., Ekshayesh, A. A., et al. (2023). Optical investigations of gold nano rods and gold nano rods doped with ZnO nanoparticles for optoelectronic applications. *Journal of Optics (India)*, *52*, 2023–2030. https://doi.org/10.1007/S12596-023-01120-1/FIGURES/10
19. Begildayeva, T., Lee, S. J., Yu, Y., et al. (2021). Production of copper nanoparticles exhibiting various morphologies via pulsed laser ablation in different solvents and their catalytic activity for reduction of toxic nitroaromatic compounds. *Journal of Hazardous Materials*, *409*, 124412. https://doi.org/10.1016/J.JHAZMAT.2020.124412
20. Patel, D. N., Pandey, S., & Bhattacharjee, S. (2018). Size-controlled growth of nanoparticles and clusters during pulsed laser ablation into an ambient wave induced plasma. *Applied Surface Science*, *462*, 373–377. https://doi.org/10.1016/j.apsusc.2018.08.051
21. Ivanov, D. S., Shakhov, P., Tikhonowsky, G., et al. (2024). Ultrafast laser ablation of gold in liquids: Effect of laser pulse overlap-induced surface porosity on size distribution of formed nanoparticles. *Applied Surface Science*, *643*, 158662. https://doi.org/10.1016/J.APSUSC.2023.158662
22. Streubel, R., Barcikowski, S., Gökce, B., et al. (2016). Continuous multigram nanoparticle synthesis by high-power, high-repetition-rate ultrafast laser ablation in liquids. *Optics Letters*, *41*, 1486. https://doi.org/10.1364/ol.41.001486
23. Streubel, R., Bendt, G., Gökce, B., et al. (2017). Pilot-scale synthesis of metal nanoparticles by high-speed pulsed laser ablation in liquids. *Nanotechnology*, *27*, 92–112. https://doi.org/10.1088/0957-4484/27/20/205602
24. Gatsa, O., Tahir, S., Flimelová, M., et al. (2024). Unveiling fundamentals of multi-beam pulsed laser ablation in liquids toward scaling up nanoparticle production. *Nanomaterials*. https://doi.org/10.3390/NANO14040365
25. Kohsakowski, S., Santagata, A., Dell'Aglio, M., et al. (2017). High productive and continuous nanoparticle fabrication by laser ablation of a wire-target in a liquid jet. *Applied Surface Science*, *403*, 487–499. https://doi.org/10.1016/j.apsusc.2017.01.077
26. Johny, J., Van Halteren, C. E. R., Zwiehoff, S., et al. (2022). Impact of sterilization on the colloidal stability of ligand-free gold nanoparticles for biomedical applications. *Langmuir, 38*, 13030–13047. https://doi.org/10.1021/acs.langmuir.2c01557
27. Gao, J., Huang, X., Liu, H., et al. (2012). Colloidal stability of gold nanoparticles modified with thiol compounds: Bioconjugation and application in cancer cell imaging. *Langmuir*, *28*, 4464–4471. https://doi.org/10.1021/la204289k
28. Sobhan, M. A., Withford, M. J., & Goldys, E. M. (2010). Enhanced stability of gold colloids produced by femtosecond laser synthesis in aqueous solution of CTAB. *Langmuir*, *26*, 3156–3159. https://doi.org/10.1021/la903088e
29. Darwish, M. I. M., Takenoshita, Y., Hamada, T., et al. (2017). Spontaneous Preparation of highly stable gold nanoparticle stabilized with ω–sulfonylated Alkylsulfanylaniline. *Journal of Oleo Science*, *66*, 1349–1354. https://doi.org/10.5650/jos.ess17151
30. Chantaramethakul, J., Choophun, N., Chokradjaroen, C., et al. (2023). Morphological evolution of gold nanoparticles synthesized via solution plasma sputtering: Effect of sodium chloride concentration and storage time. *Journal of Physical Chemistry C*, *127*, 3184–3193. https://doi.org/10.1021/acs.jpcc.2c06474
31. Aboudzadeh, M. A., Kruse, J., Sanromán Iglesias, M., et al. (2021). Gold nanoparticles endowed with low-temperature colloidal stability by Cyclic polyethylene glycol in ethanol. *Soft Matter*, *17*, 7792–7801. https://doi.org/10.1039/d1sm00720c
32. Israelachvili, J. N. (2010). Intermolecular and Surface Forces, Third Edition. Intermolecular and Surface Forces, Third Edition 1–674. https://doi.org/10.1016/C2009-0-21560-1
33. Derjaguin, B., & Landau, L. (1993). Theory of the stability of strongly charged lyophobic sols and of the adhesion of strongly charged particles in solutions of electrolytes. *Progress in Surface Science*, *43*, 30–59. https://doi.org/10.1016/0079-6816(93)90013-L
34. Merk, V., Rehbock, C., Becker, F., et al. (2014). *In situ Non-DLVO stabilization of Surfactant-Free*. E ff ect of Hofmeister ' s Anions.
35. Gregory, K. P., Wanless, E. J., Webber, G. B., et al. (2021). The electrostatic origins of specific ion effects: Quantifying the hofmeister series for anions. *Chemical Science*, *12*, 15007–15015. https://doi.org/10.1039/D1SC03568A
36. Kang, B., Tang, H., Zhao, Z., & Song, S. (2020). Hofmeister series: Insights of ion specificity from amphiphilic assembly and interface property. *ACS Omega*, *5*, 6229–6239.
37. Gregory, K. P., Elliott, G. R., Robertson, H., et al. (2022). Understanding specific ion effects and the hofmeister series. *Physical Chemistry Chemical Physics*, *24*, 12682–12718. https://doi.org/10.1039/D2CP00847E
38. Wei, W. (2023). Hofmeister effects shine in nanoscience. *Advanced Science*. https://doi.org/10.1002/ADVS.202302057
39. Ziefuß, A. R., Barcikowski, S., & Rehbock, C. (2019). Synergism between specific halide anions and pH effects during nanosecond laser fragmentation of Ligand-Free gold nanoparticles. *Langmuir*, *35*, 6630–6639.
40. Lévy, A., De Anda Villa, M., Laurens, G., et al. (2021). Surface chemistry of gold nanoparticles produced by laser ablation in pure and saline water. *Langmuir*, *37*, 5783–5794. https://doi.org/10.1021/acs.langmuir.1c00092
41. Ritzert, P., Striegel, A., & von Klitzing, R. (2025). Ion-Specific stability of gold nanoparticle suspensions. *Langmuir*, *41*, 9.
42. Zhang, Z., Li, H., Zhang, F., et al. (2014). Investigation of halide-induced aggregation of Au nanoparticles into spongelike gold. *Langmuir*, *30*, 2648–2659.
43. Christau, S., Moeller, T., Genzer, J., et al. (2017). Salt-Induced aggregation of negatively charged gold nanoparticles confined in a polymer brush matrix. *Macromolecules*, *50*, 7333–7343.
44. Caporali, S., Muniz-Miranda, F., Pedone, A., & Muniz-Miranda, M. (2019). SERS, XPS and DFT study of Xanthine adsorbed on Citrate-Stabilized gold nanoparticles. *Italian National Conference on Sensors 19*. https://doi.org/10.3390/S19122700
45. Madeira, S., Barbosa, A., Moura, C. G., et al. (2020). Aunps and Agμps-functionalized zirconia surfaces by hybrid laser technology for dental implants. *Ceramics International*, *46*, 7109–7121. https://doi.org/10.1016/j.ceramint.2019.11.203
46. De Bortoli, L. S., Vanoni, C. R., Jost, C. L., et al. (2023). Stable and ligand-free gold nanoparticles produced by laser ablation as efficient electrocatalysts for electrochemical sensing of dopamine. *Journal of Electroanalytical Chemistry*, *947*, 117744. https://doi.org/10.1016/j.jelechem.2023.117744
47. Hohenberg, P., & Kohn, W. (1964). Inhomogeneous electron gas. *Physical Review*, *136*, B864. https://doi.org/10.1103/PHYSREV.136.B864/FIGURE/1/THUMB
48. Kohn, W., & Sham, L. J. (1965). Self-consistent equations including exchange and correlation effects. *Physical Review*, *140*, A1133. https://doi.org/10.1103/PHYSREV.140.A1133/FIGURE/1/THUMB
49. Perdew, J. P., Burke, K., & Ernzerhof, M. (1996). Generalized gradient approximation made simple. *Physical Review Letters*, *77*, 3865–3868. https://doi.org/10.1103/PhysRevLett.77.3865
50. Grimme, S. (2006). Semiempirical GGA-type density functional constructed with a long-range dispersion correction. *Journal of*

Computational Chemistry, *27*, 1787–1799. https://doi.org/10.1002/JCC.20495
51. Grimme, S., Antony, J., Ehrlich, S., et al. (2010). A consistent and accurate Ab initio parametrization of density functional dispersion correction (DFT-D) for the 94 elements H-Pu. *Physical Review B - Condensed Matter and Materials Physics*, *43*, 143684. https://doi.org/10.1007/BF01322185
52. Blöchl, P. E. (1994). Projector augmented-wave method. *Physical Review B*, *50*, 17953. https://doi.org/10.1103/PhysRevB.50.17953
53. Kresse, G., & Joubert, D. (1999). From ultrasoft pseudopotentials to the projector augmented-wave method. *Physical Review B*, *59*, 1758. https://doi.org/10.1103/PhysRevB.59.1758
54. Kresse, G., & Furthmüller, J. (1996). Efficient iterative schemes for *ab initio* total-energy calculations using a plane-wave basis set. *Physical Review B, 54*, 11169. https://doi.org/10.1103/PhysRevB.54.11169
55. Kresse, G., & Hafner, J. (1993). *Ab initio* molecular dynamics for open-shell transition metals. *Physical Review B, 48*, 13115. https://doi.org/10.1103/PhysRevB.48.13115
56. Takeda, T. (1978). The scalar relativistic approximation. *Zeitschrift für Physik B Condensed Matter and Quanta, 32*, 43–48. https://doi.org/10.1007/BF01322185/METRICS
57. Zhang, C., Liu, J., Ren, Z., et al. (1977). A technique for relativistic spin-polarised calculations. *Journal of Physics C: Solid State Physics*, *10*, 3107. https://doi.org/10.1088/0022-3719/10/16/019
58. Ricardo, P. C., Serudo, R. L., Ţălu, Ş, et al. (2022). Encapsulation of Bromelain in Combined Sodium Alginate and Amino Acid Carriers: Experimental design of Simplex-Centroid mixtures for digestibility evaluation. *Molecules, 27*, Article 6364. https://doi.org/10.3390/MOLECULES27196364
59. Ray, T. R., Lettiere, B., De Rutte, J., & Pennathur, S. (2015). Quantitative characterization of the colloidal stability of metallic nanoparticles using UV-vis absorbance spectroscopy. *Langmuir, 31*, 3577–3586. https://doi.org/10.1021/la504511j
60. Mahmoud, N. N., Al-Qaoud, K. M., Al-Bakri, A. G., et al. (2016). Colloidal stability of gold nanorod solution upon exposure to excised human skin: Effect of surface chemistry and protein adsorption. *International Journal of Biochemistry & Cell Biology, 75*, 223–231. https://doi.org/10.1016/j.biocel.2016.02.020
61. Alkilany, A. M., Abulateefeh, S. R., Mills, K. K., et al. (2014). Colloidal stability of citrate and mercaptoacetic acid capped gold nanoparticles upon lyophilization: Effect of capping ligand attachment and type of cryoprotectants. *Langmuir, 30*(46), 13799–808. https://doi.org/10.1021/LA504000V
62. Palazzo, G., Valenza, G., Dell'Aglio, M., & De Giacomo, A. (2017). On the stability of gold nanoparticles synthesized by laser ablation in liquids. *Journal of Colloid and Interface Science*, *489*, 47–56. https://doi.org/10.1016/J.JCIS.2016.09.017
63. PENSA, Evangelina et al. The chemistry of the sulfur–gold interface: in search of a unified model. Accounts of chemical research, v. 45, n. 8, p. 1183-1192, 2012.
64. Saxena, I., Ehmann, K., & Cao, J. (2015). High throughput microfabrication using laser induced plasma in saline aqueous medium. *Journal of Materials Processing Technology*, *217*, 77–87. https://doi.org/10.1016/J.JMATPROTEC.2014.10.018
65. Ahmad, K., Kakakhel, M. B., Hayat, S., et al. (2021). Thermoluminescence study of pellets prepared using NaCl from Khewra salt mines in Pakistan. *Radiation and Environmental Biophysics*, *60*, 365–375. https://doi.org/10.1007/S00411-021-00894-X/FIGURES/11
66. Zheng, H., Li, Y., Shi, D., et al. (2020). Preparation and thermal property of unusual morphology NaNO3 modified by solution combustion for thermal energy storage. *Journal of Energy Storage*, *29*, 101366. https://doi.org/10.1016/J.EST.2020.101366
67. Shu, S., Huang, Y., Zou, L., et al. (2023). Mechanism of synergistic removal of NO and SO 2 by sodium bicarbonate. *RSC Advances, 13*, 32589–32595. https://doi.org/10.1039/D3RA04672A
68. Falletta, E., Rossi, M., & Della Pina, C. (2022). The versatility of gold: From heterogeneous catalysis to biomedicine. *Inorganica Chimica Acta*, *537*, 120959. https://doi.org/10.1016/J.ICA.2022.120959
69. Bhattacharjee, S. (2016). DLS and zeta potential - What they are and what they are not? *Journal of Controlled Release*, *235*, 337–351. https://doi.org/10.1016/j.jconrel.2016.06.017
70. Pochapski, D. J., Carvalho Dos Santos, C., Leite, G. W., et al. (2021). Zeta potential and colloidal stability predictions for inorganic nanoparticle dispersions: Effects of experimental conditions and electrokinetic models on the interpretation of results. *Langmuir, 37*, 13379–13389. https://doi.org/10.1021/acs.langmuir.1c02056
71. Zia, Y., Rahimi, K., Liavali, M. N., et al. (2024). Sulfite ion and gold (111) surface interaction mechanism. *Physica B Condensed Matter, 685*, 416064. https://doi.org/10.1016/J.PHYSB.2024.416064
72. Olenic, L., Mihailescu, G., Pruneanu, S., et al. (2005). Nanoparticles from a gold complex with sulfite ion as ligand: Preparation and characterization. *Particulate Science and Technology*, *23*, 79–83. https://doi.org/10.1080/02726350590886144
73. Rehbock, C., Merk, V., Gamrad, L., et al. (2013). Size control of laser-fabricated surfactant-free gold nanoparticles with highly diluted electrolytes and their subsequent bioconjugation. *Physical Chemistry Chemical Physics, 15*, 3057–3067. https://doi.org/10.1039/c2cp42641b
74. Ziefuß, A. R., Barcikowski, S., & Rehbock, C. (2019). Synergism between specific halide anions and pH effects during nanosecond laser fragmentation of ligand-free gold nanoparticles. *Langmuir, 35*, 6630–6639. https://doi.org/10.1021/ACS.LANGMUIR.9B00418
75. Mateos, H., Picca, R. A., Mallardi, A., et al. (2020). Effect of the surface chemical composition and of added metal cation concentration on the stability of metal nanoparticles synthesized by pulsed laser ablation in water. *Applied Sciences, 10*, Article 4169. https://doi.org/10.3390/APP10124169
76. Keskin, B., Üzer, A., & Apak, R. (2022). Ionic liquid-modified gold nanoparticle-based colorimetric sensor for perchlorate detection via anion – π interaction. *ACS Omega, 7*, 28065–28075. https://doi.org/10.1021/ACSOMEGA.2C02078
77. Ielo, I., Rando, G., Giacobello, F., et al. (2021). Synthesis, chemical–physical characterization, and biomedical applications of functional gold nanoparticles: A review. *Molecules, 26*, Article 5823. https://doi.org/10.3390/MOLECULES26195823
78. Filippov, S. K., Khusnutdinov, R., Murmiliuk, A., et al. (2023). Dynamic light scattering and transmission electron microscopy in drug delivery: A roadmap for correct characterization of nanoparticles and interpretation of results. *Materials Horizons*, *10*, 5354–5370. https://doi.org/10.1039/D3MH00717K
79. Kang, B., Tang, H., Zhao, Z., & Song, S. (2020). Hofmeister series: Insights of ion specificity from amphiphilic assembly and interface property. *ACS Omega*, *5*, 6229–6239. https://doi.org/10.1021/ACSOMEGA.0C00237
80. Mohrhusen, L., & Osmić, M. (2017). Sterical ligand stabilization of nanocrystals versus electrostatic shielding by ionic compounds: A principle model study with TEM and XPS. *RSC Advances*, *7*, 12897–12907. https://doi.org/10.1039/C6RA27454D
81. Muto, H., Yamada, K., Miyajima, K., & Mafuné, F. (2007). Estimation of surface oxide on surfactant-free gold nanoparticles laser-ablated in water. *Journal of Physical Chemistry C, 111*, 17221–17226. https://doi.org/10.1021/JP075582M

82. De Anda Villa, M., Gaudin, J., Amans, D., et al. (2019). Assessing the surface oxidation state of free-standing gold nanoparticles produced by laser ablation. *Langmuir, 35*, 11859–11871. https://doi.org/10.1021/ACS.LANGMUIR.9B02159
83. Intartaglia, R., Rodio, M., Abdellatif, M., et al. (2016). Extensive characterization of oxide-coated colloidal gold nanoparticles synthesized by laser ablation in liquid. *Materials, 9*(9), Article 775. https://doi.org/10.3390/MA9090775
84. Letzel, A., Gökce, B., Wagener, P., et al. (2017). Size quenching during laser synthesis of colloids happens already in the vapor phase of the cavitation bubble. *Journal of Physical Chemistry C*, *121*, 5356–5365. https://doi.org/10.1021/acs.jpcc.6b12554
85. Chopada, R., Sarwate, R., & Kumar, V. (2025). Effect of mild to extreme pH, temperature, and ionic strength on the colloidal stability of differentially capped gold nanoparticles. *Journal of Molecular Structure*, *1323*, 140751. https://doi.org/10.1016/J.MOLSTRUC.2024.140751
86. Singh-Miller, N. E., & Marzari, N. (2009). Surface energies, work functions, and surface relaxations of low-index metallic surfaces from first principles. *Physical Review B, 80*, 1–9. https://doi.org/10.1103/PhysRevB.80.235407
87. Baletto, F., & Ferrando, R. (2005). Structural properties of nanoclusters: Energetic, thermodynamic, and kinetic effects. *Reviews of Modern Physics*, *77*, 371–423. https://doi.org/10.1103/RevModPhys.77.371
88. Schmid, G., Baletto, F., Ferrando, R., & Mackay, A. L. (2008). A dense non-crystallographic packing of equal spheres. *Reviews of Modern Physics*, *15*, 1909–1930. https://doi.org/10.1107/s036510x6200239x
89. Alonso, J. A. (2000). Electronic and atomic structure, and magnetism of transition-metal clusters. *Chemical Reviews, 100*, 637–677. https://doi.org/10.1021/cr980391o
90. Da Silva, J. L. F., Kim, H. G., Piotrowski, M. J., et al. (2010). Reconstruction of core and surface nanoparticles: The example of Pt 55 and Au55. *Physical Review B, 82*, 1–6. https://doi.org/10.1103/PhysRevB.82.205424
91. dos Santos Neto, A. G., Santos, T. F., Junior, J. A., de O, et al. (2024). Combining novel theoretical and experimental insights into the physical electrochemistry of gold and carbon-based electrodes and Baicalein flavonoid sensing. *Electrochimica Acta*, *475*, 143684. https://doi.org/10.1016/j.electacta.2023.143684
92. Guan, L., Li, X., Li, Q., et al. (2009). Relaxation and electronic states of Au(100), (110) and (111) surfaces. *Solid State Communications, 149*, 1561–1564. https://doi.org/10.1016/j.ssc.2009.05.046
93. Piotrowski, M. J., Orenha, R. P., Parreira, R. L. T., & Guedes-Sobrinho, D. (2022). Assessment of the van der Waals, Hubbard U parameter and spin-orbit coupling corrections on the 2D/3D structures from metal gold congeners clusters. *Journal of Computational Chemistry, 43*, 230–243. https://doi.org/10.1002/jcc.26784
94. Zehner, M., & Gibbs, D. (1991). SANDY, A. R. et al. Structure and phases of the Au (111) surface: X-ray-scattering measurements. *Physical Review B* B, v. 43, n. 6, p. 4667, 1991.
95. Tran, R., Xu, Z., Radhakrishnan, B., et al. (2016). Surface energies of elemental crystals. *Scientific Data 2016*, *3*(1 3), 1–13. https://doi.org/10.1038/sdata.2016.80
96. CCCBDB introduction navigation https://cccbdb.nist.gov/. Accessed 15 Jan 2024.
97. Jendrzej, S., Gökce, B., Amendola, V., & Barcikowski, S. (2016). Barrierless growth of precursor-free, ultrafast laser-fragmented noble metal nanoparticles by colloidal atom clusters – A kinetic in situ study. *Journal of Colloid and Interface Science*, *463*, 299–307. https://doi.org/10.1016/J.JCIS.2015.10.032

Publisher's Note Springer Nature remains neutral with regard to jurisdictional claims in published maps and institutional affiliations.

Springer Nature or its licensor (e.g. a society or other partner) holds exclusive rights to this article under a publishing agreement with the author(s) or other rightsholder(s); author self-archiving of the accepted manuscript version of this article is solely governed by the terms of such publishing agreement and applicable law.

Doctor Philipi Cavalcante Ricardo received his PhD in Materials Science andEngineering from the Federal University of Santa Catarina (UFSC), Brazil, in 2025. Heis currently a Postdoctoral Researcher in the Department of Materials Science andEngineering at UFSC. He obtained his MSc in Materials Science and Engineering fromthe Federal University of Amazonas (UFAM), Brazil, in 2021, and his BSc in ChemicalEngineering from the State University of Amazonas (UEA), Brazil, in 2018. Hisdoctoral research was conducted within the Ceramics and Composite MaterialsResearch Group (CERMAT/UFSC). His research interests include nanomaterialssynthesis, biosensors, bioeconomy, bioprocess scale-up, and systems for encapsulationand controlled release of bioactive compounds, with a current focus on the greensynthesis of nanomaterials using pulsed laser ablation in liquids.

Doctor Caio Raphael Vanoni received his PhD in Analytical and ElectroanalyticalChemistry from the Federal University of Santa Catarina (UFSC), Brazil, in 2025,including a doctoral research period at the University of Minho, Portugal, in 2023. Hisresearch focused on the synthesis of nanomaterials by pulsed laser ablation in liquids(PLAL) and their application in modified electrochemical sensors and photosensors. Heobtained his BSc in Chemistry and Technological Chemistry from UFSC in 2016 andhis teaching degree in Chemistry from UFSC in 2023. He also holds a Bachelor'sdegree in Textile and Fashion from the University of São Paulo (USP), Brazil. Hisresearch interests include nanomaterials synthesis, electrochemical sensingtechnologies, and the characterization of energy storage devices such as supercapacitors.

Professor Maurício Jeomar Piotrowski received his BSc in Physics from the FederalUniversity of Santa Maria (UFSM), Brazil, in 2007, and his MSc (2009) and PhD(2012) in Physics from the Graduate Program in Physics at the same institution. Hecompleted postdoctoral research at the Institute of Chemistry of São Carlos, Universityof São Paulo (IQSC-USP), Brazil. He is currently a Professor in the Department ofPhysics at the Institute of Physics and Mathematics of the Federal University of Pelotas(UFPel), Brazil. His research is focused on condensed matter physics, particularly first-principles calculations, electronic structure analysis, and computational methods appliedto physics, chemistry, and materials science. His work includes the development ofadvanced materials for nanocatalysis, solar energy conversion, optoelectronic andthermoelectric devices, and molecular adsorption processes. He is especially interestedin sustainable materials such as metallic nanoclusters, two-dimensional materials, andperovskites.

Master Daniel Coutinho Costa concluded his bachelor's degree in biomedicalengineering at the Polytechnic of Porto, in 2017, and his master's degree in the samefield in 2019, at the University of Porto. Currently, he is a Ph.D. Student in BiomedicalEngineering at the Center for Microelectromechanical Systems, at the University ofMinho (CMEMSUMinho).

Doctor Jorge Padrão is a Junior Researcher at the Centre for Textile Science andTechnology (2C2T), University of Minho, Portugal. He received his degree in AppliedBiology in 2006 and his PhD in Chemical and Biological Engineering in 2014, bothfrom the University of Minho. His research is focused on advanced multifunctionaltextile base materials and the development of novel protocols for their generation andcharacterization. His work involves the development and characterization of functionaltextile materials with applications in health, automotive, aerospace, living textiles, andsustainable technologies.

Professor Andrea Zille received his degree in Environmental Sciences with aspecialization in Environmental Biochemistry from the University of Venice, Italy, in2000, and his PhD in Textile Engineering from the University of Minho, Portugal, in2005. He is currently an Associate Professor in the Department of Textile Engineeringat the University of Minho and Director of the Centre for Textile Science andTechnology (2C2T). His research focuses on biotechnology and nanotechnologyapplied to fibrous materials, particularly nanomodification of textiles for health andenvironmental applications. Since 2021, he has been listed among the World's Top 2%Scientists by Stanford University and Elsevier.

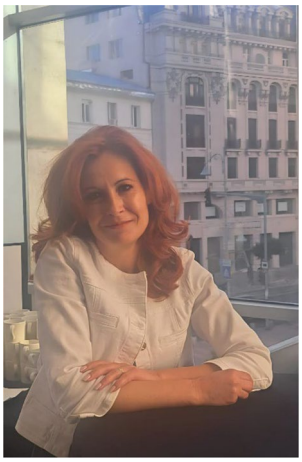

Doctor Veronica Satulu is a Scientific Researcher at the National Institute for Laser,Plasma, and Radiation Physics (INFLPR) in Romania. She received her PhD in Physicsfrom the University of Bucharest in 2011, where her research focused on the depositionof organic thin films using plasma-based techniques. Her academic background includesa bachelor's degree in Technological Physics and a master's degree in Optics,Spectroscopy, Plasma, and Lasers from the University of Bucharest. Her researchfocuses on the plasma processing of materials and the development of advancedmultifunctional materials using plasma-based technologies. The applications of herwork include modifying nuclear membranes, creating transparent conductive polymers,developing antimicrobial coatings, and advancing materials for fusion technology.

Gheorghe Dinescu is a Senior Scientist at the National Institute for Lasers, Plasma andRadiation Physics (Romania) and a PhD supervisor at the University of Bucharest.Trained as a physicist with multidisciplinary expertise in biophysics, optics,spectroscopy, lasers, and plasma physics, he conducts research in plasma science andplasma processing for material synthesis and modification at the National Institute forLaser, Plasma and Radiation Physics in Magurele, Bucharest, Romania. His workincludes gas discharges and laser-generated plasmas, synthesis of nanostructuredmaterials (metallic nanoparticles, carbon nanostructures, and polymer-metalcomposites), reactive plasma processes for thin-film deposition and surfacemodification, plasma-assisted creation of biointerfaces, and plasma applications forfusion technology.

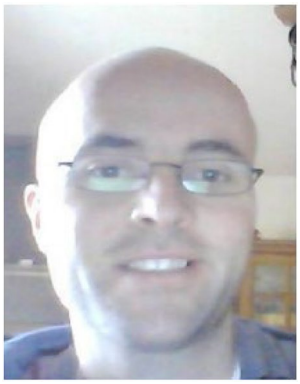

Professor Óscar Carvalho received his PhD in Mechanical Engineering and iscurrently an Associate Professor in the Department of Mechanical Engineering at theUniversity of Minho, Portugal. He has an interdisciplinary academic background withtraining in chemical, physical, and mechanical engineering. His research focuses onmaterials characterization and processing, as well as the investigation of mechanical andbiological behavior of advanced materials. His work contributes to the development andevaluation of materials for engineering and biomedical applications..

Professor Cristiane Luisa Jost is an Associate Professor in the Department ofChemistry at the Federal University of Santa Catarina (UFSC), Brazil, and leader of theAmpere. Laboratory of Electrochemical Platforms (QMC/UFSC). She received her BScin Industrial Chemistry (2003), MSc in Analytical Chemistry (2005), and PhD inAnalytical Chemistry (2010) from the Federal University of Santa Maria (UFSM),Brazil, including a research period at Constructor University (formerly JacobsUniversity Bremen), Germany. Her research focuses on electroanalytical chemistry,particularly the application of voltammetric techniques for the determination ofclinically and environmentally relevant analytes using bare and modified electrodes, aswell as screening approaches for raw materials and pharmaceutical formulations.

Professor Filipe Samuel Silva received his PhD in Mechanical Engineering and iscurrently a Full Professor in the Department of Mechanical Engineering at theUniversity of Minho, Portugal. He leads the Microfabrication and Systems IntegrationLaboratory at the Center for Microelectromechanical Systems (CMEMS). He has morethan 20 years of experience in the design and development of multifunctionalcomponents, mechanical testing, and advanced manufacturing processes. His researchfocuses on bio-related components, functionally graded materials, and bioactivematerials, with applications in biomedical engineering and advanced manufacturingtechnologies.

Professor Marcio Celso Fredel received his BSc in Mechanical Engineering (1986)and MSc in Mechanical Engineering (1990) from the Federal University of SantaCatarina (UFSC), Brazil, and his PhD from RWTH Aachen University, Germany, in1995. He is currently a Full Professor in the Department of Mechanical Engineering atUFSC and leader of the Ceramics and Composite Materials Research Center(CERMAT). His research focuses on materials and mechanical engineering, particularlynear net shape powder-based manufacturing. His work includes ceramic and compositematerials, low-temperature powder synthesis routes, laser ablation in liquids (LAL),spark plasma sintering (SPS), biomaterials, interfacial and surface energy, ballisticprotection materials, additive manufacturing, powder injection molding (PIM), andmechanical behavior analysis of engineering materials.